







Multi-Material Decomposition for Single Energy CT Using Material Sparsity Constraint

Yi Xue, Wenjian Qin, Chen Luo[®], Pengfei Yang[®], Yangkang Jiang, Tiffany Tsui, Hongjian He[®], Li Wang[®], Jiale Qin, Yaogin Xie[®], and Tianye Niu[®]

Abstract — Multi-material decomposition (MMD) decomposes CT images into basis material images, and is a promising technique in clinical diagnostic CT to identify material compositions within the human body. MMD could be implemented on measurements obtained from spectral CT protocol, although spectral CT data acquisition is not readily available in most clinical environments. MMD methods using single energy CT (SECT), broadly applied in radiological departments of most hospitals, have been proposed in the literature while challenged by the inferior decomposition accuracy and the limited number of material bases due to the constrained material information in the SECT measurement. In this paper, we propose an image-domain SECT MMD method using material sparsity as an assistance under the condition that each voxel of the CT image contains at most two different elemental materials. L₀ norm represents the material sparsity constraint (MSC) and is integrated into the decomposition objective function with a least-square data fidelity term, total variation term, and a sum-to-one

Manuscript received November 26, 2020; accepted January 9, 2021. Date of publication January 18, 2021; date of current version April 30, 2021. This work was supported in part by the National Key Research and Development Program of China under Grant 2018YFE0114800 and Grant 2019YFB1311800, in part by the Natural Science Foundation of China (NSFC) under Grant 81871351 and Grant 81827804, in part by the Zhejiang Postdoctoral Scientific Research Preferred Project under Grant zj2019004, and in part by the Key Laboratory of Orthopaedics of Zhejiang Province under Grant ZJGK1809Y. (Yi Xue and Wenjian Qin contributed equally to this work.) (Corresponding author: Tianye Niu.)

Yi Xue and Chen Luo are with the Institute of Biomedical Engineering, Shenzhen Bay Laboratory, Shenzhen 518107, China (e-mail: 11818327@zju.edu.cn; ecei@qq.com).

Wenjian Qin and Yaoqin Xie are with the Shenzhen Institutes of Advanced Technology, Chinese Academy of Sciences, Shenzhen 518055, China (e-mail: wj.qin@siat.ac.cn; yq.xie@siat.ac.cn).

Pengfei Yang is with the School of Biomedical Engineering and Instrument Science, Zhejiang University, Hangzhou 310027, China (e-mail: p-fly@zju.edu.cn).

Yangkang Jiang is with the Sir Run Run Shaw Hospital, Zhejiang University School of Medicine, Hangzhou 310029, China, and also with the Institute of Translational Medicine, Zhejiang University, Hangzhou 310009, China (e-mail: 11718077@zju.edu.cn).

Tiffany Tsui and Tianye Niu are with the Nuclear & Radiological Engineering and Medical Physics Programs, Woodruff School of Mechanical Engineering, Georgia Institute of Technology, Atlanta, GA 30332 USA (e-mail: ttsui38@gatech.edu; tyniu@gatech.edu).

Hongjian He is with the Key Laboratory for Biomedical Engineering of Ministry of Education, Center for Brain Imaging Science and Technology, College of Biomedical Engineering and Instrumental Science, Zhejiang University, Hangzhou 310029, China (e-mail: hhezju@zju.edu.cn).

Li Wang is with the Department of Mathematics, University of Texas at Arlington, Arlington, TX 19408 USA (e-mail: li.wang@uta.edu).

Jiale Qin is with the Women's Hospital, Zhejiang University School of Medicine, Hangzhou 310006, China (e-mail: qinjiale0625@163.com). Digital Object Identifier 10.1109/TMI.2021.3051416

constraint of material volume fractions. An accelerated primal-dual (APD) algorithm with line-search scheme is applied to solve the problem. The pixelwise direct inversion method with the two-material assumption (TMA) is applied to estimate the initials. We validate the proposed method on phantom and patient data. Compared with the TMA method, the proposed MSC method increases the volume fraction accuracy (VFA) from 92.0% to 98.5% in the phantom study. In the patient study, the calcification area can be clearly visualized in the virtual non-contrast image generated by the proposed method, and has a similar shape to that in the ground-truth contrast-free CT image. The high decomposition image quality from the proposed method substantially facilitates the SECT-based MMD clinical applications.

Index Terms— Multi-material decomposition, single energy CT, material sparsity, two-material assumption.

I. INTRODUCTION

THE interest grows in the development of multi-material decomposition (MMD) technique, which differentiates the material compositions within the human body by decomposing the CT images into multi-material bases [1]–[4]. The decomposed materials can be used in the clinical applications, such as lesion delineation, organ contour, virtual monoenergetic synthesis, virtual non-contrast (VNC) imaging, liver fibrosis quantification, bone mineral quantitative determination [5]–[8], etc.

The implementation of MMD can be classified into single-energy CT (SECT) based and spectral CT based schemes according to the various procedures in CT data acquisition [9]–[12]. In the spectral CT measurement, hardware modification of the CT scanner is required, including using multiple scans [13], changing fast x-ray tube voltage [14], scanning with dual-source [15], [16], using dual-layer [17] or photon counting detector scheme [4], employing primary modulation [15], [18], etc.

The efficacy of spectral CT has been demonstrated in some clinical applications while the hardware modulation presents a major obstacle toward the extensive applications of spectral CT in clinic. SECT, however, is omnipresent in almost all hospitals. SECT based MMD, without the need of any hardware modification, is thus more attractive in the clinic. Important advances have been made in the development of the SECT based material decomposition method in the past few years. Liao *et al.* applied a cascade deep convolutional

1558-254X © 2021 IEEE. Personal use is permitted, but republication/redistribution requires IEEE permission. See https://www.ieee.org/publications/rights/index.html for more information.

neural network (CD-ConvNet), which combines a material decomposition layer and a noise suppression layer, to enhance the decomposition performance [19]. This method was validated using patient data to decompose the bone and softtissue. Nevertheless, it has to perform material-specific neural network training for a dedicated material basis. The multiple training operation limits the application of the algorithm. Currently, Zhao et al. applied U-net on the SECT image to generate the corresponding dual-energy CT (DECT) images and performed material decomposition using the acquired DECT data [20]. This U-net based method is successfully validated in virtual non-contrast imaging, which is an important diagnostic imaging application of material decomposition. The deep learning-based material decomposition method is burdened by a large amount of training data. Additionally, multi-material images require labeling before operation, but accurate label generation is still an on-going problem.

In addition to the deep learning-based SECT material decomposition method, Kis et al. proposed a two-pass SECT two-material decomposition method using the x-ray total path length estimation [9]. This method reconstructs the CT image from the original projections using a standard FDK algorithm and then calculates the x-ray path length using the ray tracing algorithm. The x-ray total path length, which is the sum of path lengths of two materials, is utilized in the decomposition algorithm as a known constraint. Combining the total path length constraint and the projection measurement, two sets of material images are successfully estimated. Crawley et al. analyzed the accuracy of SECT in bone mineral measurements, which relies on the linear correlation between the in-vivo concentrations of calcium hydroxyapatite and dipotassium phosphate [8]. These two methods successfully achieved dual-material decomposition using SECT while their clinical application is hindered by the inferior decomposition accuracy and the limited number of decomposed materials [9]. This is because MMD for SECT is an ill-posed problem that has to estimate multiple sets of material images from one measurement. An accurate solution cannot be acquired if no additional information is included.

In medical imaging, each voxel in the CT image contains a limited number of materials, indicating that the material composition in each voxel is sparse. We can design a material sparsity constraint to assist in the MMD for SECT. L₀ norm, which counts the number of non-zero elements in one vector, has been introduced in image processing to regularize the image gradient sparsity [21]–[23]. L₀ norm minimizes the number of voxels that have non-zero gradient magnitudes rather than the total image gradient magnitude to better preserve the spatial resolution of the CT image. In this work, we apply the L₀ norm directly on the regularization of material composition to achieve the material sparsity in each voxel.

In addition to the L₀ norm that regularizes material sparsity constraint, the proposed image-domain MMD method for SECT formulates the objective function using a least-square data fidelity term, a total variation (TV) term based on the piecewise constant property of the material image to suppress the magnified noise in the decomposition [24], and a characteristic function to satisfy the sum-to-one constraint of the decomposed material volume fractions. The proposed objec-

tive function is non-convex due to the L_0 norm regularization. An accelerated primal-dual (APD) algorithm with line-search scheme is applied to solve the problem [25]. To acquire a good initial value for the non-convex problem, we applied the pixelwise direct matrix inversion method with the assumption that each pixel contains at most two materials.

In essence, the main technical innovation of the proposed method is to introduce the concept of material sparsity into the decomposition to enhance decomposition accuracy. L_0 norm is selected as an embodiment of material sparsity due to its definition of counting the number of non-zero elements in one vector. The proposed method serves as an alternative option to the clinical applications where DECT or spectral CT is not readily available. The proposed method is evaluated using digital phantoms, customized water phantoms, and the patient data.

II. METHODS AND MATERIALS

A. MMD Mathematical Model Using SECT

In the image domain MMD theory, the mass attenuation of a mixture $\mu_M(E)$ in the CT image is assumed to be a linear combination of the mass attenuation of different material bases and written as [26]:

$$\mu_{M}(E) = \sum_{t=1}^{T_{0}} \beta_{t} \mu_{tM}(E), \quad s.t. \sum_{t=1}^{T_{0}} \beta_{t} = 1, \beta_{t} \ge 0,$$
(1)

where $\mu_{tM}(E)$ is the mass attenuation coefficient of the *t*-th basis material at the energy level *E*. The subscript *M* indicates the mass attenuation coefficient. T_0 represents the total number of material bases. β_t is the mass fraction of the *t*-th basis material written as:

$$\beta_t = \frac{m_t}{\sum_{t=1}^{T_0} m_t},\tag{2}$$

where m_t is the mass of the t-th basis material.

The relationship between the linear attenuation coefficient (LAC) μ_E and mass attenuation coefficient μ_M is expressed as:

$$\mu_E = \rho \mu_M (E) = \frac{\sum_{t=1}^{T_0} m_t}{\sum_{t=1}^{T} V_t} \mu_M(E), \tag{3}$$

where V_t is the volume of the t-th basis material. Combining Eqs. (1) and (2) into Eq. (3), we have:

$$\mu_E = \sum_{t=1}^{T_0} \left(\frac{\sum_{t=1}^{T_0} m_t}{\sum_{t=1}^{T_0} V_t} \frac{m_t}{\sum_{t=1}^{T_0} m_t} \frac{V_t \mu_{tE}}{m_t} \right) = \sum_{t=1}^{T_0} \mu_{tE} x_t, \tag{4}$$

where $x_t = \frac{V_t}{\sum_{t=1}^{T_0} V_t}$ represents the volume fraction of the *t*-th basis material and μ_{tE} is the LAC of the *t*-th basis material. x_t satisfies the sum-to-one and bound between 0 and 1:

$$\sum_{t=1}^{T_0} x_t = \sum_{t=1}^{T_0} \frac{V_t}{\sum_{t=1}^{T_0} V_t} = 1, \quad 0 \le x_t \le 1, \ t = 1, \dots, T_0.$$
(5)

The MMD model can be constructed from Eqs. (4) and (5)

$$\mu_E = \sum_{t=1}^{T_0} x_t \mu_{tE}, \quad \text{s.t. } \sum_{t=1}^{T_0} x_t = 1, \ x_t \ge 0, \ \forall t.$$
 (6)

To implement the MMD in the CT image of N_p pixels, Eq. (6) is rewritten in the matrix-vector form as:

$$\overrightarrow{\mu} = A\vec{x}, \quad s.t. \ \sum_{t=1}^{T_0} x_t = 1, \ x_t \ge 0, \ \forall t,$$
 (7)

where $\overrightarrow{\mu}$ is the measured CT images after reordering the data as a column vector. Similarly, $\vec{x} = \begin{bmatrix} \overrightarrow{x_1}^T, \overrightarrow{x_2}^T, \dots, \overrightarrow{x_{T_0}}^T \end{bmatrix}^T$ is a column vector with size $T_0 \times N_p$, where entry is the volume fraction image of the *t*-th basis material. $A \in \mathbb{R}^{N_p \times T_0 N_p}$ is the material composition matrix and is written as:

$$A = A_0 \otimes I_{N_p}, \tag{8}$$

where \otimes represents the Kronecker product. I_{N_p} is the $N_p \times N_p$ identity matrix. $A_0 = \begin{bmatrix} \mu_1, \mu_2, \dots \mu_{T_0} \end{bmatrix}$ is the composition matrix composed of the LACs of the material bases.

Performing MMD is mathematically equivalent to solving the volume fraction \vec{x} from Eq. (7), given the measured CT image $\overrightarrow{\mu}$. The solutions to the SECT MMD equation produce non-unique solutions since multiple solutions \vec{x} can be estimated from one measurement $\overrightarrow{\mu}$. The pseudo-inverse A^{-1} is mathematically unstable and thus Eq. (7) cannot be solved using the direct matrix inversion since the severe crosstalk error may occur in the decomposed images.

Least square estimation with regularization is commonly applied to solve the above ill-posed inverse problem. We formulate the image domain SECT MMD problem as:

$$\frac{\min}{\vec{x}} \frac{1}{2} \|A\vec{x} - \overrightarrow{\mu}\|_{2}^{2} + \delta \|\vec{x}\|_{TV} + \sigma \|\vec{x}\|_{0} + \chi s(\vec{x}).$$
(9)

The first term is the data fidelity term and $\|\blacksquare\|_2^2$ denotes the square of a L₂-norm operator. The data fidelity term enforces the minimization between the linear combination of volume fractions of the estimated and the measured CT images. The second term $\|\blacksquare\|_{TV}$ denotes the TV of each material image [24]. This term is based on the hypothesis that different materials in the CT image can be considered as a piecewise constant [27]. The hypothesis might be valid in the phantom study while may expire in sophisticated patient data evaluation. The minimization of the TV term achieves noise suppression in the material image while maintaining the major edges of the object. The TV term is calculated using the L₁ norm of the material gradient image, i.e.,

$$\|\vec{x}\|_{TV} = \|\nabla \vec{x}\|_1 = \sum_{t=1}^{T_0} \|\nabla \vec{x_t}\|_1,$$
 (10)

where ∇ represents the gradient operator. The third term $\|\vec{x}\|_0$ represents the L₀ norm of the material image \vec{x} and $\|\blacksquare\|_0$ is a L₀ norm operator. This term limits the number of material types within human organs using the sparsity constraint on the material volume fraction \vec{x} [3], [4]. $\|\vec{x}\|_0$ is calculated as:

$$\|\vec{x}\|_0 = \sum_{p=1}^{N_p} \|\vec{x}_p\|_0,$$
 (11)

where $\overrightarrow{x_p}$ is the vectorized volume fraction of the *p*-th pixel, i.e., $\overrightarrow{x_p} = (x_{p1}, x_{p2}, \dots, x_{pT_0})^T$. The final term $\chi s(\overrightarrow{x})$ is the

characteristic function which includes the sum-to-one and box constraints, i.e., Eq. (5), and is calculated as:

$$\chi s\left(\vec{x}\right) = \begin{cases}
0, & \overrightarrow{x_p} \in S, \ \forall p \\
\infty, & otherwise,
\end{cases}$$
(12)

where $S = \{\overrightarrow{x_p}: \sum_{t=1}^{T_0} x_{pt} = 1, 0 \le x_{pt} \le 1, p = 1, 2, \dots, N_p\}$. Note that, the major clinical applications using the proposed method are the water solution of various contrast agents, including the Iodine-based contrast, Gadolinium-based contrast, and non-dissolving materials. The volume conservation assumption is usually satisfied in these studies. The scenarios where volume conservation is not met are commonly involved with the dissolving process of solid or high-concentration liquid materials, which are not readily observed in clinical practice. The parameter δ is utilized to achieve the tradeoff between image noise and spatial resolution. σ is the regularization parameter to tune the weights of material sparsity. A larger σ enforces a fewer number of material types within each pixel. We refer to the proposed SECT MMD scheme as the material sparsity constrained (MSC) method hereafter.

B. Optimization Method

We utilize an APD algorithm with a line-search scheme to solve the problem, i.e., Eq. (9) [25]. The advantage of the APD algorithm is the accelerated convergence rate when compared against conventional methods including the forward-backward method [28] and the alternating direction method of multipliers (ADMM) algorithm [29]. This primal-dual algorithm solves the optimization problems of the canonical form [25]:

$$\min_{x} f(z) + g(x), \quad s.t. \ z = Kx, \tag{13}$$

where K is a linear operator. f and g are expected to be convex functions [25]. In medical imaging inverse problems, these convex requirements are usually breached without ending in catastrophic results [30]-[33]. It has been shown experimentally that the primal-dual splitting method for convex optimization is applicable in the nonconvex setting despite missing theoretical support. In this work, we propose an empirical algorithm to solve the non-convex problem.

To solve the image domain SECT MMD problem of Eq. (9), we define f and g using the following equations to split Eq. (9) into three convex functions and one non-convex function as:

$$\begin{cases} f_1\left(\overrightarrow{z_1}\right) = \frac{1}{2} \left\|\overrightarrow{z_1} - \overrightarrow{\mu}\right\|_2^2, & (14\text{-}1) \\ f_2\left(\overrightarrow{z_2}\right) = \delta \left\|\overrightarrow{z_2}\right\|_1, & (14\text{-}2) \\ f_3\left(\overrightarrow{z_3}\right) = \chi s\left(\overrightarrow{z_3}\right), & (14\text{-}3) \end{cases}$$

$$f_2\left(\overrightarrow{z_2}\right) = \delta \left\|\overrightarrow{z_2}\right\|_1,$$
 (14-2)

$$f_3\left(\overrightarrow{z_3}\right) = \chi s\left(\overrightarrow{z_3}\right),$$
 (14-3)

$$g(\vec{x}) = \sigma \|\vec{x}\|_0,$$
 (14-4)

where $\overrightarrow{z_1} = A\overrightarrow{x}$, $\overrightarrow{z_2} = \nabla \overrightarrow{x}$, $\overrightarrow{z_3} = \overrightarrow{x}$ and the linear operator K is expressed as $K = [A, \nabla, I]^T$.

The optimization algorithm is composed of outer and inner iterations. The outer iteration updates the material image by mapping the estimated difference to the constrained sparse solution pool using a proximal operation. An inner iteration performs the line-search scheme to find a sufficiently large step

size with guaranteed convergence for the outer iteration. The major operation of APD algorithm is to calculate the convex conjugate of f which is referred to as f^* hereafter and the proximal operators of f^* and g. The proximal operator of a general function h is defined as [33]:

$$prox_{rh}(\vec{x}) = \underset{\vec{w}}{argmin} \left(h(\vec{w}) + \frac{1}{2r} \|\vec{w} - \vec{x}\|_{2}^{2} \right), \quad (15)$$

where \vec{x} is the dual variable of \vec{w} . The step size r controls the extent to which the proximal operator maps points towards the minimum of the function h. [34].

We apply the hard thresholding technique to solve the proximal operator of g [35] and the projection onto hypercube to solve the proximal operator of f_2^* . Moreau decomposition scheme is performed on the conjugate operators of f_1^* and f_3^* to translate the calculation into the proximal operators of original functions f_1 and f_3 [36], [37]. The proximal maps of f_1 and f_3 are eventually solved using the extreme value property of a quadratic function and projection onto simplex operation. The details are shown in the following.

Using Eq.(15), the proximal operator of function g (Eq. (14-4)) is written as:

$$prox_{lg}(\vec{x}) = \frac{argmin}{\vec{w}} \left(\sigma \|\vec{w}\|_0 + \frac{1}{2t} \|\vec{w} - \vec{x}\|_2^2 \right), \quad (16)$$

where t is the step size of the proximal operator of g. Eq. (16) is a non-convex problem due to the L_0 norm. To solve Eq. (16), we apply the hard thresholding technique as proposed in ref. [35] to approximate the proximal map of g as:

$$(prox_{tg}(\vec{x}))_i = \begin{cases} (\vec{x})_i & if \ |(\vec{x})_i| \ge \sqrt{2\sigma t} \\ 0 & otherwise, \end{cases}$$
 (17)

where $(\vec{x})_i$ is the *i*-th element in the vectorized variable \vec{x} .

We define s as the step size of the proximal operator of f^* , the convex conjugate of function f. The proximal operator of conjugate function f_2^* is written as:

$$\operatorname{prox}_{sf_{2}^{*}}\left(\overrightarrow{w_{2}}\right) = \frac{\operatorname{argmin}}{\overrightarrow{z_{2}}} \left(f_{2}^{*}\left(\overrightarrow{z_{2}}\right) + \frac{1}{2s} \left\| \overrightarrow{z_{2}} - \overrightarrow{w_{2}} \right\|_{2}^{2} \right). \tag{18}$$

We derive an explicit expression of $f_2^*(\overline{z_2})$ as:

$$f_2^* \left(\overrightarrow{z_2} \right) = \begin{cases} 0 & if \ \| \overrightarrow{z_2} \|_{\infty} \le \delta \\ \infty & otherwise. \end{cases}$$
 (19)

The derivation detail of the f_2^* function can be found in Appendix A. By plugging Eq. (19) into Eq. (18), the minimum of Eq. (18) is reached when $\overrightarrow{w_2} = \overrightarrow{z_2}$ and $f_2^* (\overrightarrow{z_2}) = 0$. The final form of the proximal map of conjugate function f_2^* is thus written as:

Instead of directly solving for the proximal operators of f_1^* and f_3^* which involves the tedious calculation of conjugate functions, we apply the Moreau decomposition scheme on these conjugate operators to translate the calculation into the

proximal operator of original functions f_1 and f_3 . The Moreau decomposition is defined as [38]:

$$prox_{sf^*}(\vec{w}) + s \times prox_{s^{-1}f}\left(\frac{\vec{w}}{s}\right) = \vec{w}.$$
 (21)

By plugging the definition of f_1 (Eq.14-1) into Eq. (21), the proximal operator of f_1^* using Moreau decomposition is written as:

$$prox_{sf_1^*}(\overrightarrow{w_1}) = \frac{\overrightarrow{w_1} - s\overrightarrow{\mu}}{1+s}.$$
 (22)

Details of the derivation of the f_1^* proximal operator can be found in Appendix B.

The proximal operator of f_3^* using Moreau decomposition is written as:

$$prox_{sf_3^*}(\overrightarrow{w_3}) = \overrightarrow{w_3} - s \times prox_{s^{-1}f_3}(\frac{\overrightarrow{w_3}}{s}).$$
 (23)

Here $prox_{s^{-1}f_3}\left(\frac{\overline{w_3}}{s}\right)$ can be solved using the projection onto a simplex scheme proposed in refs. [36], [37] as:

$$\left(prox_{s^{-1}f_3}\left(\frac{\overrightarrow{w_3}}{s}\right)\right)_i = \begin{cases} \frac{\left(\overrightarrow{w_3}\right)_i}{s} - \hat{t} & if \frac{\left(\overrightarrow{w_3}\right)_i}{s} \ge \hat{t}, \\ 0 & otherwise \end{cases}$$
(24)

where *i* is the index of the *i*-th element in \overrightarrow{w}_3 . \hat{t} and *k* are defined as:

$$\begin{cases}
\hat{t} := \frac{1}{n-k} \left(\sum_{j=k+1}^{n} \left(\frac{\overrightarrow{w_3}}{s} \right)_{(j)} - 1 \right), & (25-1) \\
k := \left\{ p : \left(\frac{\overrightarrow{w_3}}{s} \right)_{(p+1)} \ge \frac{1}{n-k} \left(\sum_{j=p+1}^{n} \left(\frac{\overrightarrow{w_3}}{s} \right)_{(j)} - 1 \right) \right\}, & (25-2)
\end{cases}$$

where $\left(\frac{\overrightarrow{w_3}}{s}\right)_{(1)} \leq \ldots \leq \left(\frac{\overrightarrow{w_3}}{s}\right)_{(n)}$ is the permutation of $\left(\frac{\overrightarrow{w_3}}{s}\right)$ in an ascending order. Combining Eqs. (23), (24) and (25), we acquire the proximal map of f_3^* as:

$$\left(prox_{sf_3^*}\left(\overrightarrow{w_3}\right)\right)_i = \begin{cases} s\hat{t} & if \left(\overrightarrow{w_3}\right)_i \ge s\hat{t} \\ \left(\overrightarrow{w_3}\right)_i & otherwise \end{cases}. \tag{26}$$

The pseudocode of the APD algorithm is included from Lines 22 to 44 in Table I.

C. Initial Value Estimation

Eq. (7) for the p-th pixel can be re-written as:

$$A_0 \overrightarrow{x_p} = \overrightarrow{\mu_p}, \quad s.t. \ \sum_{t=1}^{T_0} x_{pt} = 1, \ x_{pt} \ge 0, \ \forall t,$$
 (27)

where $A_0 = \left[\mu_1, \mu_2, \dots \mu_{T_0} \right]$ is a $1 \times T_0$ matrix and the accurate inversion A_0^{-1} does not exist. We obtain the LAC of the material basis by manually selecting a uniform region of interest (ROI) in the CT image that contains the material bases and calculating the mean value in the ROI as the entry of the matrix A_0 in all the stuies. This method is verified by other researchers in medical imaging research [1], [26], [39], [40]. We assume that each pixel is composed

TABLE I
THE PSEUDOCODE OF THE PROPOSED METHOD

line	program
1	***Initial value generation using the proposed TMA-SECT method***
2	// μ_p is the LAC of the <i>p</i> -th pixel; P is the total number of pixels.
3	$// \mu_t^{basis}$ is the LAC of the <i>t</i> -th basis material.
4	$//\tau_c$ is the c-th two-material candidate.
5	// C is the total number of material candidates.
6	$//(i,j)$ is the <i>i</i> -th and <i>j</i> -th material basis in the material candidate l_c .
7	for $p = 1$:P $count = 0$; //the variable $count$ counts the number of feasible
8	solutions
9	for $c = 1:C$
10	$\begin{bmatrix} x_{pi} \\ x_{pj} \end{bmatrix} = \begin{bmatrix} \mu_i & \mu_j \\ 1 & 1 \end{bmatrix}^{-1} \begin{bmatrix} \mu_p \\ 1 \end{bmatrix}$
11	$ \mathbf{if} x_{ni}, x_{ni} \ge 0 $
12	count = count + 1;
13	end
14	end
15 16	if count > 0 // Multiple solutions exist // Calculate the Euclidean distance
17	$\tau_{c}^{*} _{\tau_{c}^{*}=(l^{*}J^{*})} = \underset{\tau_{c}=(l,j)}{\arg\min} \sqrt{\left\ \mu_{p}-\mu_{l}\right\ ^{2} + \left\ \mu_{p}-\mu_{j}\right\ ^{2}};$
18	$x_p^* = (x_{pi^*}, x_{pj^*})^T;$
19	else //No feasible solution
20	Use GP method to solve:
	$ (\tau_c^*, x_{pi}^* x_{pj}^*) = \underset{\substack{\tau_c = (i,j) \\ x_{pi} x_{pj}}}{\min} $
21	$x_{pi}x_{pj}$
	$s.t. \begin{cases} x_{pi} \ge 0 \\ x_{pi} \ge 0 \end{cases}$
	$x_p^* = (x_{pi^*}, x_{pj^*})^T;$
22	end
23 24	end Output: $\vec{x}^0 = \text{col}(x_1^*, x_2^*,, x_n^*)^T$ //Initial value
24	Output: $x = \operatorname{col}(x_1, x_2, \dots, x_p)$ // initial value
25	***MSC using APD algorithm with a line-search scheme***
26	Input: $\vec{x}^0 = \text{col}(x_1^*, x_2^*,, x_p^*)^T$
27	// Initialization $\overline{w_1}^0 = A\vec{x}^0, \overline{w_2}^0 = \nabla \vec{x}^0, \overline{w_3}^0 = \vec{x}^0$
28	$w_1 = Ax^{\gamma}, w_2 = vx^{\gamma}, w_3 = x^{\gamma}$ $t^0 > 0, v \in [0,1], \beta^0 > 0, \theta^0 := 1, \gamma > 0$
29	// Main iteration
30	for $k = 1, 2, 3$
31	$\overrightarrow{w}^{k-1} := \left[\overrightarrow{w_1}^{k-1}, \overrightarrow{w_2}^{k-1}, \overrightarrow{w_3}^{k-1}\right]^T$ $K := [A, \nabla, I]^T \qquad \text{//Linear operator}$ $\overrightarrow{x^k} := \overrightarrow{x}^{k-1} - t^{k-1} K^T \overrightarrow{w}^{k-1}$
32	$K := [A, \nabla, 1]^T$ //Linear operator
33	$\dot{x}^{\kappa} := \dot{x}^{\kappa-1} - t^{\kappa-1} K^{T} \dot{w}^{\kappa-1}$ //Hard thresholding
33	$(\widehat{\vec{v}^k})$ if $ \widehat{\vec{v}^k} > \sqrt{2\sigma t^{k-1}}$
22	$(\hat{x}^{\kappa})_i \coloneqq \begin{cases} \begin{pmatrix} x & j_i & x & x = x \\ 0 & \text{otherwise} \end{cases}$
34	$ \begin{aligned} (\vec{x}^k)_i &\coloneqq \left\{ \begin{pmatrix} \vec{\hat{x}^k} \rangle_i & \text{if } \left (\vec{\hat{x}^k})_i \right \ge \sqrt{2\sigma t^{k-1}} \\ 0 & \text{otherwise} \end{aligned} \right. \\ \beta^k &\coloneqq \beta^{k-1} (1 + \gamma t^{k-1}) \end{aligned} $
35	Choose any $t^k \in \left[t^{k-1} \sqrt{\frac{\beta^{k-1}}{\beta^k}}, t^{k-1} \sqrt{\frac{\beta^{k-1}}{\beta^k}} (1 + \theta^{k-1})\right]$
36	
37	Repeat //Line search of optimal updating step $\theta^k := \frac{t^k}{t^{k-1}}$
38	$egin{aligned} artheta &\coloneqq rac{t^{k-1}}{t^k} \ \widehat{ec{x}}^k &\coloneqq \vec{x}^k + heta^k (\vec{x}^k - \vec{x}^{k-1}) \end{aligned}$
38 39	$s^k := \beta^k t^k$
40	$\widehat{w_1}^k := \overline{w_1}^{k-1} + s^k A \widehat{x}^k, \overline{w_1}^k := \frac{\widehat{w_1}^k - s^k \overline{\mu}}{1 + s^k}$
70	$W_1 \coloneqq W_1 + S^*Ax^k, W_1 \coloneqq \frac{1}{1+s^k}$
	$\left \left(\overline{w_2^{n}}\right)_i if \left \left(\overline{w_2^{n}}\right)_i\right \leq \delta$
41	$\overrightarrow{w_2}^k := \overrightarrow{w_2}^{k-1} + s^k \nabla \widehat{x}^k, \ (\overrightarrow{w_2}^k)_i = \begin{cases} -\delta & if \ (\overrightarrow{w_2}^k) < -\delta \end{cases}$
	$\widehat{w_{2}}^{k} := \overline{w_{2}}^{k-1} + s^{k} \nabla \widehat{x^{k}}, \ (\overline{w_{2}}^{k})_{i} = \begin{cases} \left(\widehat{w_{2}}^{k}\right)_{i} & \text{if } \left \left(\widehat{w_{2}}^{k}\right)_{i}\right \leq \delta \\ -\delta & \text{if } \left(\widehat{w_{2}}^{k}\right)_{i} < -\delta \\ \delta & \text{otherwise} \end{cases}$ $\widehat{w_{3}}^{k} := \overline{w_{3}}^{k-1} + s^{k} I \widehat{x^{k}}, \ (\overline{w_{3}}^{k})_{i} := \begin{cases} s^{k} \widehat{t} & \text{if } \left(\widehat{w_{3}}^{k}\right)_{i} \geq s^{k} \widehat{t} \\ \left(\widehat{w_{3}}^{k}\right)_{i} & \text{otherwise} \end{cases}$
	$\left(s^k\hat{t} \text{ if } \left(\widehat{w_s}^k\right) > s^k\hat{t}\right)$
42	$\overline{w_3}^k \coloneqq \overline{w_3}^{k-1} + s^k I \widehat{x}^k, \ (\overline{w_3}^k)_i \coloneqq \begin{cases} 3 & \text{or } i \leq 3 \end{cases}$
	$\left(\left(\overrightarrow{W_3}^{\wedge}\right)_i\right)$ otherwise
43	$\overrightarrow{W}^{k} = [\overrightarrow{W_{1}}^{k}, \overrightarrow{W_{2}}^{k}, \overrightarrow{W_{3}}^{k}]^{T}$ $P_{1} = (\overrightarrow{W_{1}}^{k}, \overrightarrow{W_{2}}^{k}, \overrightarrow{W_{3}}^{k})^{T} + (\overrightarrow{W_{1}}^{k}, \overrightarrow{W_{2}}^{k}, \overrightarrow{W_{3}}^{k})^{T}$
44 45	Break if $\sqrt{\beta^k} t^k K^T(\vec{w}^k - \vec{w}^{k-1}) _2 \le (\vec{w}^k - \vec{w}^{k-1}) _2$
45 46	$t_k \coloneqq t_k * v$ end
47	end

of at most two materials. Similar assumption is utilized in refs [1], [26], [41]–[44]. Under this assumption, MMD defined in this manuscript refers to decomposing the whole CT image volume, rather than each pixel, into multiple material images. The two-material assumption is expressed as:

$$\sum\nolimits_{t=1}^{T_0} I_{\{x_{tp} \neq 0\}} \leq 2, \quad \forall p, \tag{28}$$

where $I_{\{\blacksquare\}}$ denotes an indicator function which equals 1 if the t-th material exists and 0 otherwise. The composition matrix for a two-material candidate $\tau = (i, j)$ can be rewritten by including the constraint (Eq. (26)) into A_0 as:

$$A' = \begin{bmatrix} \mu_i & \mu_j \\ 1 & 1 \end{bmatrix}, \tag{29}$$

where μ_i and μ_j are the LACs of the *i*-th and *j*-th basis materials, respectively. The two-material decomposition of the *p*-th pixel can be written as:

$$\begin{bmatrix} \mu_i & \mu_j \\ 1 & 1 \end{bmatrix} \begin{bmatrix} x_{pi} \\ x_{pj} \end{bmatrix} = \begin{bmatrix} \mu_p \\ 1 \end{bmatrix}, \quad s.t. \ x_{pi} \ge 0, \quad x_{pj} \ge 0.$$
(30)

Eq.(30) is initially solved using the direct matrix inversion since the determinant of A' is not equal to zero. The MMD can be achieved by looping over all the two-material candidates with the total number of $C_{T_0}^2$ options and picking up the optimal solution with the minimal Euclidean distance between the LACs of the current pixel and the material bases. The distance is calculated as:

$$\tau^* = \arg\min_{\tau = (i,j)} \sqrt{\|\mu_p - \mu_i\|^2 + \|\mu_p - \mu_j\|^2}.$$
 (31)

If no direct solution to Eq.(30) exists, the optimal one is estimated by minimizing the least-square form of Eq.(30) as:

$$\begin{pmatrix} \tau^*, x_{pi}^* x_{pj}^* \end{pmatrix} = \arg \min_{\substack{\tau = (i,j) \\ x_{pi}, x_{pj}}} \left\| \begin{bmatrix} \mu_i & \mu_j \\ 1 & 1 \end{bmatrix} \begin{bmatrix} x_{pi} \\ x_{pj} \end{bmatrix} - \begin{bmatrix} \mu_p \\ 1 \end{bmatrix} \right\|_2,$$

$$s.t. \begin{cases} x_{pi} \ge 0 \\ x_{pj} \ge 0 \end{cases}. (32)$$

Eq. (32) can be solved using, *e.g.*, the gradient projection (GP) algorithm [45]. The pseudocode to calculate the initial value is presented from Lines 1 to 24 in Table I.

D. Implementation Details

We name the proposed initial decomposition method based on the Two-Material Assumption as the TMA method. The proposed MSC method is combined with the TMA initial estimation to solve the non-convex objective function (Eq. (9)).

The pseudocode of the proposed method is summarized in Table I, where the CT images and decomposed material images are denoted by vector signs, and the symbol: = means assignment operation. The initial value is generated using the proposed TMA method as shown in Lines 1-24. In Lines 15-18 of the multiple solutions case, the optimal

		Phantom composition	Scan and reconstruction parameters				
Digital phantom	Label	Material	Ratio	Energy	# of photons	Geometry	
#1	ROI1/ROI2/ ROI3/ROI5	Bone/ Muscle/ Adipose/Air	1	50 keV	Inf	SID/SAD (mm): 1500/1000 Projection number: 676	
#2: elliptical four-material phantoms	ROI4	Muscle-adipose	0.5:0.5	$ \begin{array}{c} 1 \times 10^{3} \\ 1 \times 10^{4} \\ 1 \times 10^{5} \end{array} $		Detector size (mm): 1024×768 Detector pixel size (mm): 0.388×0.388	
#3: elliptical five-material phantom ROI1/ROI2/ ROI3/ROI4/ ROI7 ROI5 ROI6		Bone/Muscle/ Adipose/Iodine/Air Muscle-adipose Iodine-Muscle	1 0.5:0.5 0.6:0.4	1 × 10°		Image size (mm): 512×512 Image pixel size (mm): 0.5×0.5 Long/short axis (mm): 220/160	
#4: round material	ROI1/ROI2/ROI3/ ROI4	Iohexol/CaCl ₂ /Water/Air	1	100 keV		(elliptical) Diameter: 200 (round)	
phantom				on and $CaCl_2$ solution in the 7 phantoms 3.74% 1.85% 0.06%			
Water phantom	Label	Material	Ratio	Scan and reconstruction parameters			
	ROI1/ROI2/ ROI3/ROI4	Iohexol/Gadodiamide /CaCl ₂ Solution/Water	1				
#1 with IGC	ROI5	Iohexol:Water	0.8:0.2	SID/SAD (mm): 820/620		D (mm): 820/620	
insets	ROI6	Iohexol:Water	0.7:0.3	Projection number: 601			
	ROI7	Gadodiamide:CaCl ₂	0.7:0.3	Tube voltage (kVp): 75 (IGC)/100 (IG)			
	ROI1/ROI2	Iohexol/Gadodiamide	1	Tube current(mA): 60 Physical size (mm): 75/70 Detector/pixel size (mm): 2048×2048/0.154×0.154 Image/pixel size (mm): 512×512/0.15×0.15			
#2 with IG	ROI3	Iohexol:water	0.5:0.5				
insets	ROI4	Gadodiamide:Water	0.5:0.5				
Contrast-free #3	ROI	Water	1				
Clinical data	ROI composition: Contrast agent/water/calcification Scan parameter: SID/SAD (mm):1085/595; Tube energy (kVp): 80/120; Current(mA): 99; Slice thickness(mm): 5; Image/Pixel size (mm): 512×512/0.68×0.68						

TABLE II

DATA ACQUISITION AND RECONSTRUCTION PARAMETERS

material candidate is selected by minimizing the Euclidean distance between the current pixel and the material bases. In Lines 19-22, if no feasible solution exists, the optimal solution is estimated by minimizing Eq. (30). Lines 25-47 are the proposed MSC scheme which is solved using the APD algorithm with line-search scheme. k is the index of iteration. The hard thresholding operation is performed in Line 33. In the optimization, an inner iteration performs the line-search scheme to find a sufficiently large step size with guaranteed convergence for the outer iteration. The line-search scheme starts from selecting a trial step size and decreasing the step size by multiplying a factor less than one in each inner iteration. The line-search scheme jumps out the inner iteration when it reaches the stopping criteria of the convergence requirement by the APD algorithm as shown in Line 44.

III. EVALUATION

A. Data Acquisition

We evaluated the proposed method using digital phantoms, customized water phantoms, and a set of patient data. We design two elliptical digital phantoms composed of four to five materials commonly observed in patient imaging to evaluate the proposed method, and a series of round digital phantoms composed of four materials to find the critical relative LAC difference value such that the accurate material decomposition can be achieved using the proposed method. We simulate the elliptical digital phantom using the imaging

protocol of 75 kVp. The energy spectra of incident x-ray photons are simulated using the Siemens simulator [46]. A virtual 12-mm aluminum filter is placed to harden the x-ray beam. The round digital phatom is simulated using 110 keV. The monoenergetic protocol is simulated to avoid the beam-hardening effect. The LACs of basis materials are obtained from the National Institute of Standards and Technology (NIST) database [47]. The source to detector distance (SID) and source to axis distance (SAD) are 1500 mm and 1000 mm, respectively. We generate 676 projections within $[0^{\circ}, 360^{\circ})$ on the detector composed of 1024×768 pixels. The standard FDK algorithm is applied to reconstruct the volumetric data from the projections [48], [49]. In addition to a noiseless study, we have applied additive Poisson noise in the data measurements of the elliptical digital phantom using 1×10^3 , 1×10^4 and 1×10^5 incident number of x-ray photons in each detector pixel to mimic the scanning protocols from low to high doses. The experiment details of the digital phantom are shown in Table II.

To further evaluate the proposed method on the physical data, we apply the water solution of iohexol ($C_{19}H_{26}I_3N_3O_9$), gadodiamide ($C_{16}H_{26}GdN_5O_8$) and calcium chloride ($CaCl_2$) to customize a water phantom with the IGC material inserts. The four materials are mixed in different proportions and inserted into six rods fixed in a plastic water container of 75 mm diameter. The water phantom with IGC inserts is scanned using the DECT protocol of our lab-built cone-beam CT (CBCT) system as shown in Fig. 1. The CBCT



Fig. 1. The lab-built CBCT system.

system employs a rotation stage (DMT130N, OWIS Co., www.owis.eu), an x-ray tube (Rad94, Varian Medical Systems, www.varian.com) of 125kVp and a flat panel detector (1800RF, Careray Corp., cn.careray.com) with an isotropic pixel size of 0.154 mm in two dimensions. To suppress the scatter photons, a collimator (R-301, Dandong Keda Instrument Co., Ltd, www.ddkdyq.com) is placed in front of the x-ray tube to limit the z-direction coverage to be within 10 mm. An aluminum sheet of 3 mm thickness is placed in front of the x-ray exit window to harden the x-ray spectrum. In addition to the hardware filtration, we apply a two-step correction method previously developed in our group as a preprocessing operation to further alleviate the beam hardening artifacts [50]. This method models the nonlinear polychromatic attenuation process of the x-ray projection by re-projecting a template image with the estimated polychromatic spectrum. By adding the scaled difference between the monochromatic and polychromatic reprojection data to the one without correction, the raw projection data are mapping into the corresponding monochromatic domain to achieve the correction. The corrected projections are reconstructed to generate a high-quality CT image using the standard FDK algorithm [48], [49]. The experiment details of the phantom with IGC inserts are shown in Table II.

Under the same experimental condition as the water phantom with the IGC material inserts, we further apply the water solution of iohexol and gadodiamide as the contrast agent to customize a water phantom with the IG material inserts. The materials are mixed in different proportions and inserted into four test tubes fixed in a plastic water container of 70 mm in diameter. We also customize a contrast-free water phantom with the same geometric dimensions as the water phantom with the IG inserts. The only difference between the water phantom with the IG inserts and the contrast-free water phantom is that all the four test tubes are replaced with pure water. The phantom details are shown in Table II.

To demonstrate the clinical relevance using the proposed method, we further perform a patient study. The data of the patient who is scheduled for the abdominal scan in our hospital are acquired on a SOMATOM Force scanner (www.healthcare.siemens.com/). A contrast-free and a contrast-enhanced scan are obtained using the standard clinical protocol of 80 kVp and 120 kVp, respectively. The scanning and reconstruction parameters of the patient data set are summarized in Table II.

All the MMD operations are performed using Matlab on a computer installed with a 4th Generation Intel®CoreTMi7-5960X @ 3.00GHz with eight cores.

B. Comparison Study

A classical separate low-pass filtration method, which suppresses the decomposition noise using the TMA method as the initialization [51], [52], is performed to evaluate the spatial resolution maintaining the capability of the proposed MSC method. The image noise standard deviation (STD) using the low-pass filtration method is kept at the same level as that using the proposed MSC method.

We remove the L_0 norm from the proposed method and preserve the TV regularization term. This method is named as TV method and designed for comparison with the proposed method to evaluate the performance of L_0 norm. Additionally, we further compare the proposed method with our previously proposed MMD method, which enhances the decomposition spatial resolution and decreases the decomposition noise by utilizing the edge-preserving (EP) regularization in the decomposition, to demonstrate the performance of L_0 norm [43].

To evaluate the decomposition accuracy of the proposed method with respect to noise fluctuation, we apply the proposed MSC method on the simulated digital phantoms with three various levels of additive Poisson noise in the measurement. We apply consistent parameters in the decomposition of the three sets of noisy digital phantom study. The TMA method is utilized to initialize the optimization.

To evaluate the convergence and sensitivity of the proposed method on the initial value, we multiply the initial value generated by TMA method with a factor of zero, 50% and 70% in the noiseless digital phantom study, and zero, 50% and 100% in the noisy four- and five- material phantom studies with the incident number of photons of 1×10^4 in each detector pixel, equivalent to a normal dose CT scan in the clinical setting [53].

Finally, we perform a four-material digital phantom study to investigate the impact of the TV regularization parameter δ and L_0 regularization parameter σ . We tune one parameter while keeping the other one intact to investigate the individual contribution. TMA initialization is applied in the studies. The incident photon number is also set as 1×10^4 in each detector pixel to mimic the normal dose.

C. Evaluation Metrics

To evaluate decomposition accuracy and decomposed image quality of the digital phantom and water phantom, we calculate the volume fraction accuracy and the average STD on the decomposed images. The volume fraction accuracy (VFA) of the decomposition is defined as [33]:

$$VFA = (1 - \frac{1}{T_0} \sum_{t=1}^{T_0} \frac{\left| x_t^{truth} - \overline{x}_t \right|}{x_t^{truth}}) \times 100\%, \quad (33)$$

where x_t^{truth} is the volume fraction of the ground truth for the t-th material and \overline{x}_t is the mean value within a uniform ROI for the t-th material image.

The modulation transfer function (MTF) in the water phantom study is measured to investigate the decomposed image spatial resolution using the low-pass filtration method and the proposed MSC method [54]. The line spread function (LSF) is calculated using the gradient of the object edge profile and

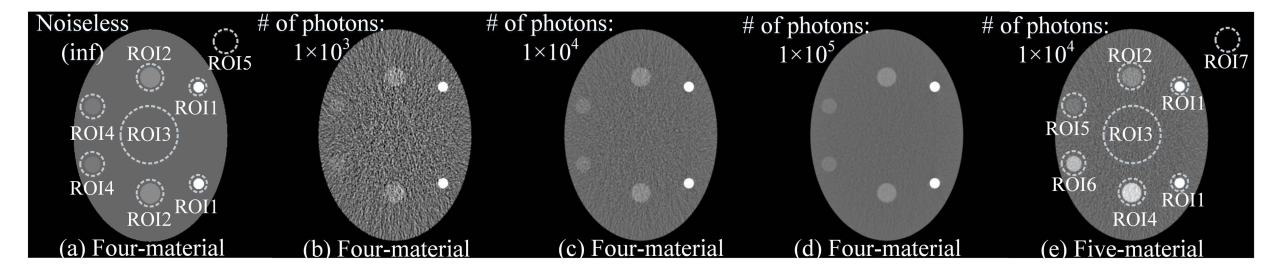


Fig. 2. CT images of the simulated elliptical digital phantoms listed in Table II. Four-material phantoms: (a) noiseless, (b) 1×10^3 , (c) 1×10^4 and (d) 1×10^5 . Five-material phantom: (e) 1×10^4 photons. Display window is [0.01 0.03] mm⁻¹. Material composition in the selected ROIs are listed in Table II.

is transferred to MTF using the Fourier transform. We average the profile of adjacent boundaries to acquire the resultant MTF with the minimal fluctuation due to image noise. The measured frequencies at MTF magnitude decreased to 0.5 (-3dB) are compared to evaluate the relative spatial resolution [55].

We further perform VNC imaging in the water phantom study and patient study using the decomposed images to demonstrate the accuracy of the proposed method. VNC imaging is an image postprocessing technique to subtract the contrast agent from the contrast-enhanced CT image to replace additional and traditional non-contrast CT scan. Currently, VNC is mostly achieved using DECT technology. In this paper, we implement VNC using SECT to acquire the decomposed materials and substitute the contrast agent by the water with the same volume fraction. The VNC image is synthesized by the linear combination of the substituted materials at a given pixel p and energy E as:

$$\mu_p^{VNC}(E) = x_{pt_1}(E)\mu_{t_2}(E) + \sum_{\substack{t=1\\t\neq t_1}}^{T_0} x_{pt}(E)\mu_t(E), \quad (34)$$

where the t_1 -th material refers to the contrast agent and the t_2 -th material refers to the water [56].

In the evaluation of the water phantom data, the root-mean-square-relative error (RMSRE (%)) of the CT number are summarized to quantify the accuracy of VNC generated using the proposed method.

The RMSRE is calculated as:

RMSRE(%) =
$$\sqrt{\frac{1}{T_0} \sum_{t}^{T_0} \left(\frac{\left| (\mu)_t - \left(\mu^{truth} \right)_t \right|}{\left(\mu^{truth} \right)_t} \right)^2} \times 100\%,$$
(35)

where $(\mu)_t$ is the average CT number of the *t*-th material in the VNC image and $(\mu^{truth})_t$ is the true CT number of the *t*-th material calculated in the contrast-free image. T_0 denotes the total number of decomposed materials.

IV. RESULTS

A. Digital Phantom Study

1) Noiseless Four-Material Phantom Study: The noiseless elliptical digital phantom involving four different components are shown in Fig. 2(a). The decomposed results are shown in Fig. 4(a). The brightness in the decomposed image indicates the volume fraction intensity of each basis material. The materials are successfully decomposed regardless of the initial

value. For quantitative analysis, we calculate the means of the volume fraction of the decomposed material images in the selected ROIs. STDs are all zero due to the noiseless simulation. The results are summarized in Table III. Though initialized with different values including zero, 50% TMA and 70% TMA, the proposed method achieves similar volume fraction accuracy (VFA), *i.e.*, 98.80%, 99.56% and 99.46%. This observation indicates that the proposed method is not susceptible to the initial estimates in the noiseless four-material elliptical digital phantom study.

We further plot out the logarithmic objective function of the proposed method with different initializations to show the stability in the convergence. The result is shown in Fig. 5(a). The objective function values using the initializations of zero, 50% TMA and 70% TMA are all converged after a certain number of iterations. The cost functions using zero and 50% TMA present large oscillations in the convergence while that of 70% TMA is more stable. The decomposition results using zero initialization before and after the oscillation as pointed by the arrow in Fig. 5(a) are shown in Fig. 5(c). The decomposition accuracy of the muscle image after the oscillation is significantly improved compared with that before the oscillation, indicating that the optimization might jump out of the local minimum after the oscillation. The logarithmic display of the objective function reveals that solving the nonconvex L₀ norm without a good initial value might be unstable. A desired initial estimate contributes to the convergence stability in the non-convex optimization algorithm.

2) Digital Phantom Studies With Additive Poisson Noise: The four-material and five-material elliptical digital phantoms are shown in Figs. 2(c) and 2(e), respectively. The corresponding decomposed basis material images are shown in Figs. 4(b) and 4(c). For quantitative evaluation, we calculate the means and STDs of the volume fraction of the decomposed material images in the selected ROIs. The results are summarized in Table III. In the four-material study, the materials are successfully decomposed regardless of the initial value. Though initialized with different values including zero, 50% TMA and 100% TMA, the proposed MSC method achieves comparable volume fraction accuracy (VFA), i.e., 97.66%, 98.47% and 98.80% as the ground truth. This observation indicates that the proposed MSC method does not depend on the initial estimates in the four-material digital phantom study. In the five-material study, when the proposed method is initialized with 50% TMA and 100% TMA images, the material

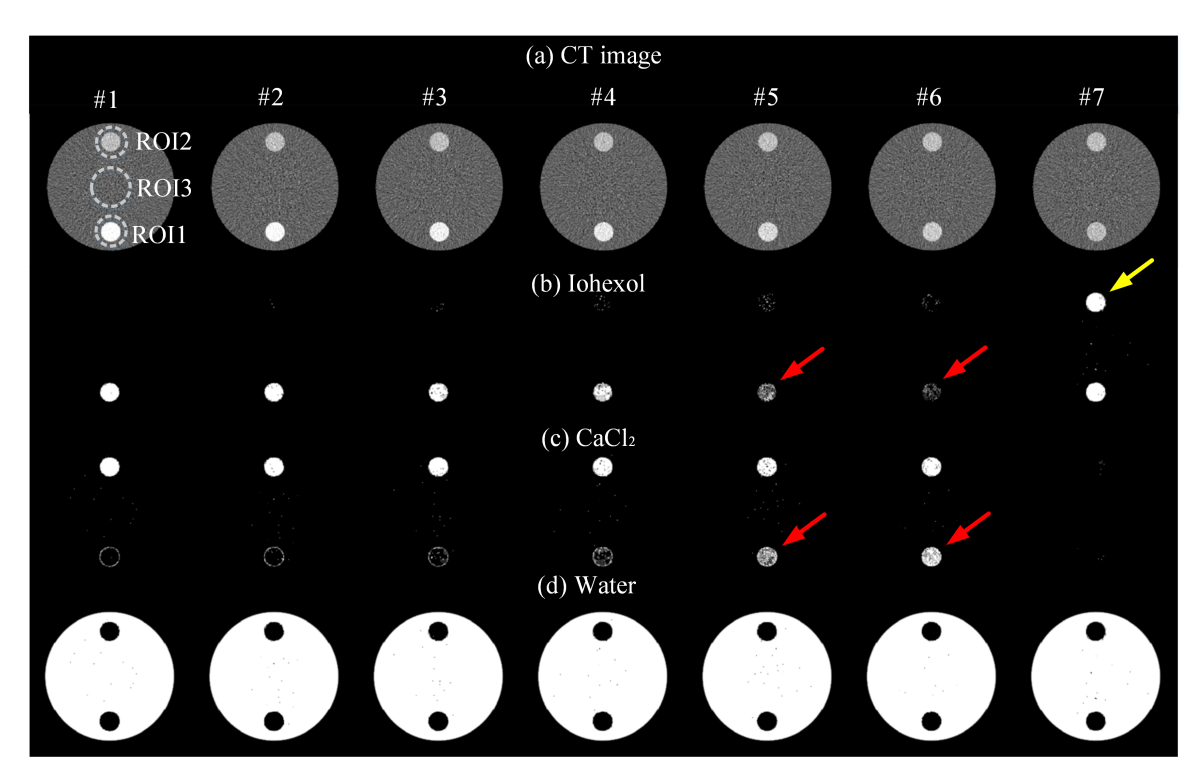


Fig. 3. The decomposed materials of (b) ioxehol solution, (c) CaCl₂ solution and (d) water decomposed from (a) the CT image of the round digital phantom #4. From #1 to #7, the LAC relative difference between iohexol solution and CaCl₂ solution is 13.71%, 11.86%, 9.15%, 6.90%, 3.74%, 1.85% and 0.06%, respectively. ROI1, ROI2 and ROI3 indicate the rod of ioxehol solution, CaCl₂ solution and water, individually. The display windows for the CT image and the decomposed material are [0.014 0.022] mm⁻¹ and [0.1], respectively.

bases are successfully decomposed. When the initialization is zero, the iodine solution, adipose, and muscle cannot be differentiated. The proposed MSC method initialized with 50% TMA and 100% TMA has comparable VFA, *i.e.*, 95.56% and 97.12% while that of zero initialization has much lower VFA. This observation indicates that the proposed MSC method is not susceptible to the initial value of less than 50% error relative to the TMA in the five-material phantom study.

As shown in Fig. 4(b6) and (c4). Cross contamination is observed in the decomposed muscle and adipose images using the EP and TV method. While in the decomposition result of the proposed method, the cross contamination is significantly suppressed. In the quantitative results of Table III, the EP, TV and proposed method all effectively suppress the decomposition noise. The VFAs are 93.49% and 98.80% using the EP and proposed method in the four-material study, and 67.31% and 95.56% using the TV and proposed method in the five-material study, respectively. The decomposition accuracy using the proposed method with L₀ norm is improved compared with that using EP and TV methods. The above observations show that the proposed material sparsity represented by L₀ norm increases the decomposition accuracy.

We plot the objective function of the proposed method in a logarithmic format with different initialization to observe the algorithm's convergence in the four-material elliptical digital phantom study with the incident number of photons of 1×10^4 in each detector pixel. The results are shown in Fig. 5(b). The cost function using the initialization of zero, 50% TMA and 100% TMA are all converged after a certain

number of iterations. The cost function using zero image shows severe oscillations in the optimization while those using 100% TMA and 50% TMA initializations are more stable. This oscillation phenomenon of objective function reveals that solving the non-convex L_0 norm without a good initial value may be unstable. A desired initial estimation helps with the convergence stability of the optimization algorithm.

3) Sensitivity Study on Penalty Parameters: We perform a four-material elliptical digital phantom study to investigate the impact of the TV regularization parameter δ and L_0 regularization parameter σ . We tune one parameter while keeping the other one intact to investigate the individual contribution. 100% TMA initialization is applied in all the studies. The incident photon number is set as 1×10^4 to mimic the normal dose. The CT image in the decomposition is shown in Fig. 2(c).

The decomposed muscle images of the proposed method using TV regularization parameter $\delta=1.5\times10^{-06},\,1.5\times10^{-08}$ and 1.5×10^{-09} are shown in Fig. 6(a). The quantitative results are summarized in Table IV. The corresponding mean STDs of the decomposition result are 0.0060, 0.1387 and 0.1414, respectively. The decomposition noise increases by around 23 times with the descending of the parameter δ by three orders of magnitude. The observation indicates that noise in the decomposition is not sensitive to the selection of the TV regularization parameter.

The decomposition results of the proposed method using the L_0 norm parameter $\sigma=0.023,\ 0.025$ and 0.026 are shown in Fig. 6(b). $\sigma=0.025$ achieves the best decomposition

	Мє	ethods	Truth	0	Proposed	50% TMA	Proposed	70% TMA	70% TMA	Proposed
Noiseless phantom #1	ROI1	Bone	1	0	1	0.5	1	0.7	0.7	1
	ROI2	Muscle	1	0	1	0.5	1	0.7	0.7	1
	ROI3	Adipose	1	0	1	0.5	1	0.7	0.7	1
	ROI4	Adipose	0.5	0	0.518	0.25	0.507	0.35	0.35	0.508
		Muscle	0.5	0	0.482	0.25	0.493	0.35	0.35	0.492
	ROI5	Air	1	0	1	0.5	1	0.7	0.7	1
	VFA			0.00%	98.80%	50.00%	99.56%	70.00%	70.00%	99.46%
	Mε	ethods	Truth	0	Proposed	50% TMA	Proposed	100% TMA	100% EP	Proposed
	ROI1	Bone	1 ± 0	0 ± 0	1±0	0.227 ± 0.246	1±0	0.958 ± 0.022	0.948 ± 0.011	1±0
Naiss form	ROI2	Muscle	1 ± 0	0 ± 0	1±0	0.441 ± 0.071	0.996 ± 0.027	0.868 ± 0.16	0.913 ± 0.037	1±0
Noisy four- material	ROI3	Adipose	1±0	0 ± 0	1±0	0.445 ± 0.059	0.995 ± 0.032	0.883 ± 0.142	0.952 ± 0.038	1±0
	ROI4	Muscle	0.5 ± 0	0 ± 0	0.535 ± 0.018	0.28 ± 0.129	0.479 ± 0.122	0.516 ± 0.2	0.523 ± 0.036	0.518 ± 0.142
phantom	RO14	Adipose	0.5 ± 0	0 ± 0	0.465 ± 0.018	0.22 ± 0.129	0.521±0.122	0.484 ± 0.2	0.477 ± 0.036	0.482 ± 0.142
(1×10^4) #2	ROI5	Air	1 ± 0	0±0	1±0	0.493±0.008	1±0	0.985 ± 0.016	0.986 ± 0.009	1±0
	1	/FA		0.00%	97.66%	43.40%	98.47%	93.81%	93.49%	98.80%
	Methods		Truth	0	Proposed	50% TMA	50% TV	Proposed	100% TMA	Proposed
	ROI1 Bone		1±0	0±0		0.488±0.013	0.763 ±		0.977±0.027	1±0
	11011 2011	0.79 ± 0.004			0.000		1±0			
	ROI2 Muscle	1±0				$0.564 \pm$			0.894 ± 0.134	
				0 ± 0	0.295 ± 0.055	0.388 ± 0.089	0.000	0.919 ± 0.117	0.775±0.179	
	ROI3	Adipose	1 ± 0	0±0	0.258 ± 0.019	0.455 ± 0.05	0.494 ± 0.03	1±0	0.911 ± 0.1	1±0
NI : C	ROI4	Iodine	1 ± 0	0		0.461±0.035	$0.557 \pm$	4		1±0
Noisy five- material phantom (1×10 ⁴) #3				0 ± 0	0.253 ± 0		0.003	1±0	0.921 ± 0.069	
	ROI5	Muscle 0.5±0	0.10	0.220+0	0.225+0.105	0.335±	0.420+0.000	0.460+0.21	0.463 ± 0.138	
		4 1:	0.5.0	0±0	0.338±0	0.235±0.105	0.032	0.438±0.098	0.469±0.21	0.527+0.120
		Adipose	0.5 ± 0	0 ± 0	0.36 ± 0.003	0.265 ± 0.105	0.37 ± 0.032	0.562±0.098	0.53±0.211	0.537±0.138
	RO6	Iodine	0.6 ± 0	0±0	0.273±0.034	0.311±0.052	0.408 ± 0.003	0.583±0.005	0.622±0.103	0.601 ± 0.008
		Muscle	0.4 ± 0	0±0	0.293±0.027	0.189 ± 0.052	0.3 ± 0.003	0.417±0.005	0.378±0.103	0.399 ± 0.008
	ROI7	Air	1±0				$0.839\pm$			1±0
		/FA	1-0	0±0 0.00%	1±0 57.56%	0.49±0.007 47.47%	0.002 67.31%	1±0 95.56%	0.98±0.014 92.80%	97 12%

TABLE III
THE MEANS AND STDS OF THE DECOMPOSED IMAGES WITHIN EACH ROLIN THE DIGITAL PHANTOM STUDY

performance. The muscle in the mixture cannot be differentiated when $\sigma=0.023$ and 0.026 as pointed by the yellow arrow in Figs. 6(b1) and (b3). The pure muscle is incorrectly decomposed when $\sigma=0.026$ as pointed by the red arrow in Fig. 6(b3). This observation indicates that decomposition is sensitive to the L₀ norm penalty parameter σ . A delicate selection of the parameter σ is required to find a desirable solution.

4) Sensitivity Study on Noise: To evaluate the proposed method using various imaging doses, we generate three sets of measurements using a different number of incident x-ray photons in each detector pixel, including 1×10^3 , 1×10^4 and 1×10^5 , to mimic the scanning protocols from low to high doses. The CT images of the elliptical digital phantom are shown in Figs. 2(b) to 2(d) with the corresponding noise STDs of 3.4×10^{-3} , 1×10^{-3} and 3.1×10^{-4} . We keep all the parameters in the optimization, including TV and L₀ norm regularization parameters, the same in the decomposition of the three sets of data. TMA is applied to initialize the optimization. The decomposition muscle results are shown from Fig. 6(c1) to 6(c3). The decomposition noise increases as the photon number decreases. When the photon number is decreased to 1×10^3 in each detector pixel, severe noise and cross-contamination could be observed.

5) Critical Relative LAC Difference Study: In the round digital phantom #4, we keep the concentration of CaCl₂ solution

unchanged and tune the concentration of iohexol fraction such that the LAC relative difference between iohexol solution and CaCl₂ solution varies from 0.06% to 13.71%. In the seven round digital phantoms labeled from #1 to #7, the LAC relative difference between iohexol solution and CaCl₂ solution in each phantom is 13.71%, 11.86%, 9.15%, 6.90%, 3.74%, 1.85% and 0.06%, respectively. The reconstructed digital phantom is shown in Fig. 3(a).

The decomposition results using our proposed method are shown in Figs. 3(b), (c) and (d). In the 5th and 6th columns of Fig. 3 (corresponding to 3.74% and 1.85% relative LAC difference), the iohexol solution is incorrectly decomposed to the CaCl₂ images as pointed by the red arrow. In the 7th column of Fig. 3 (corresponding to 0.06% relative LAC difference), the CaCl₂ material is incorrectly decomposed to the iohexol image as pointed by the yellow arrow. These observations indicate that the materials with close LAC cannot be differentiated.

To find the critical relative LAC difference value such that the accurate material decomposition can be achieved using the proposed method, we calculate the VFA of the decomposition result from the 1^{st} to the 7^{th} columns of Fig. 3 and plot the fitting curve between VFA and relative LAC difference in the digital phantom study. The VFA versus relative LAC difference is fitted using smoothing spline curve with the fitting sum of squares error (SSE) of 8.5×10^{-4} and R-square

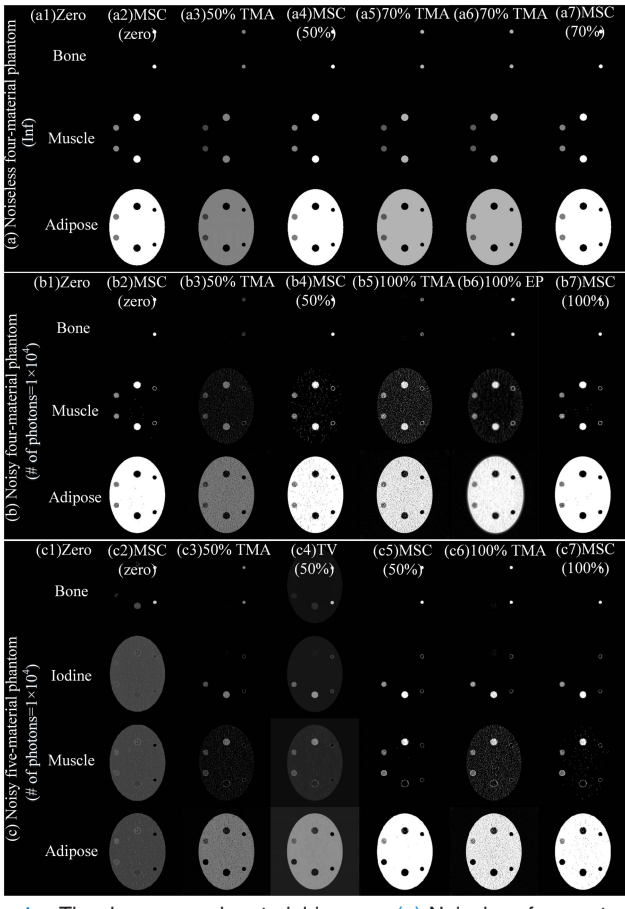


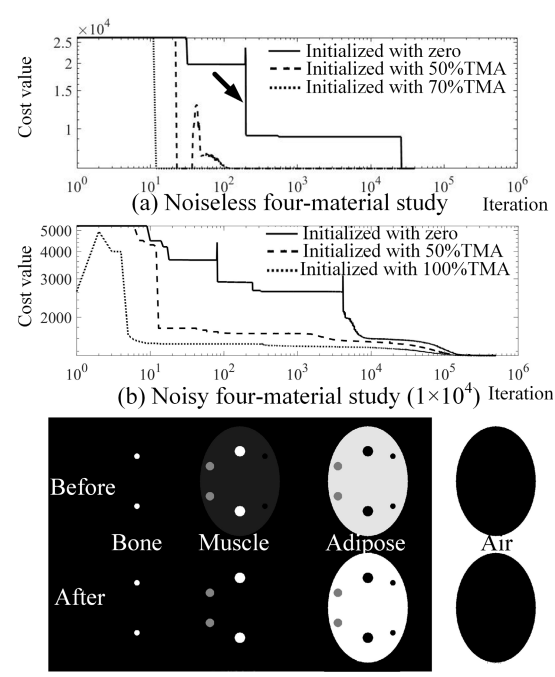
Fig. 4. The decomposed material images. (a) Noiseless four-material digital phantom study. Noisy digital phantom studies (# of photons = 1×10^4): (b) four materials and (c) five materials. (a1), (a3) and a(5), b(1), b(3) and b(5), c(1), c(3) and c(6) are the initialization images in the noiseless study and noisy studies, respectively. a(2), a(4) and a(7), b(2), b(4) and b(7), and c(2), c(5) and c(7) are the corresponding material images using the proposed MSC in the noiseless and noisy studies. b(6) and c(4) are the material images using EP method and TV method, respectively. The display window is set as [0 1] for all.

of 0.9968. The fitted result is shown in Fig. 7. When the relative LAC difference is 7.1%, the VFA is equal to 95%. The VFA drops rapidly when the relative LAC difference is less than 7.1% and maintains a high level when more than 7.1%. We conclude that the critical relative LAC difference value to achieve accurate material decomposition using the proposed method is 7.1% in the round digital phantom study.

B. Water Phantom Study

1) Water Phantom With IGC Inserts: The CT image of the water phantom is shown in Fig. 8. The decomposed basis material images are shown in Fig. 9. The proposed TMA method initially decomposes the CT image into five material images. On the basis of the TMA method, the proposed MSC scheme further suppresses the decomposition noise while maintaining the material boundary.

For quantitative analysis, ROIs in Fig. 8 are selected to calculate the decomposed material volume fraction and STD. The results are summarized in Table V. The proposed MSC method achieves a high decomposition accuracy with a VFA of 97.73%. Additionally, all the mixture regions including



1313

(c) Decomposed images before and after the oscillation pointed by the arrow in (a)

Fig. 5. The logarithmic values of the objective function using the proposed method with different initializations in: (a) noiseless four-material elliptical digital study, and (b) noisy four-material elliptical digital study (number of photons = 1×10^4). (c) shows the decomposed material images before and after the oscillation pointed by the arrow in (a).

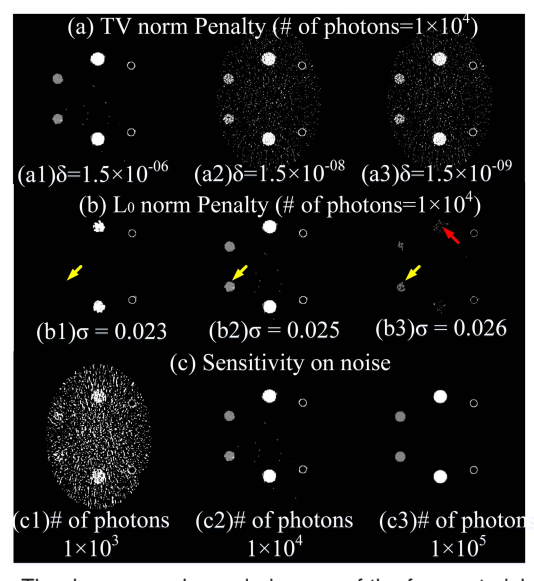


Fig. 6. The decomposed muscle images of the four-material elliptical digital phantom using various penalty parameters and incident number of photons. (a) TV penalty parameter $\delta=(1)$ 1.5 \times 10 $^{-06}$, (2) 1.5 \times 10 $^{-08}$ and (3) 1.5 \times 10 $^{-09}$. (b) L0 penalty parameter $\sigma=(1)$ 0.023, (2) 0.025 and (3) 0.026. (c) Different incident number of photons: (1) 1 \times 10 3 , (2) 1 \times 10 and (3) 1 \times 10 5 . The display windows are set as [0 1] for all.

ROI5, ROI6 and ROI7 are successfully decomposed, which shows the mixture decomposition capability of the proposed MSC method.

The average STD using MSC method is decreased by 67.45% compared with its counterparts using the TMA method. The VFA is accordingly increased by 2.94%. The comparison indicates better noise suppression using the

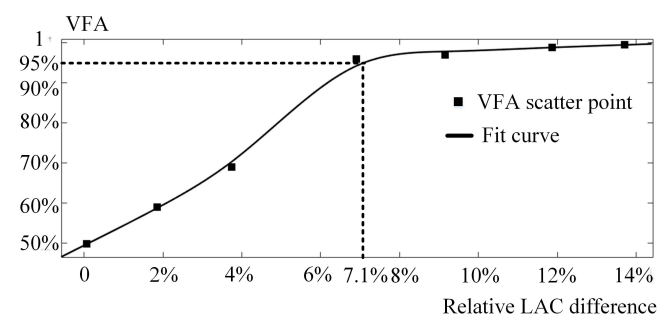


Fig. 7. The fitting curve f VFA versus relative LAC difference in the digital phantom study.

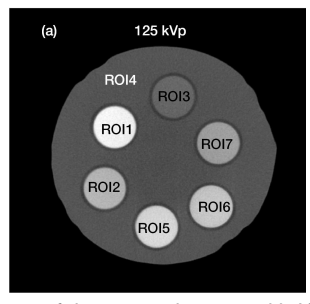


Fig. 8. DECT images of the water phantom with IGC inserts scanned on the lab-built CBCT system using the protocols of 125 kVp and 60 mA. The display window is [0.010 0.040] mm⁻¹.

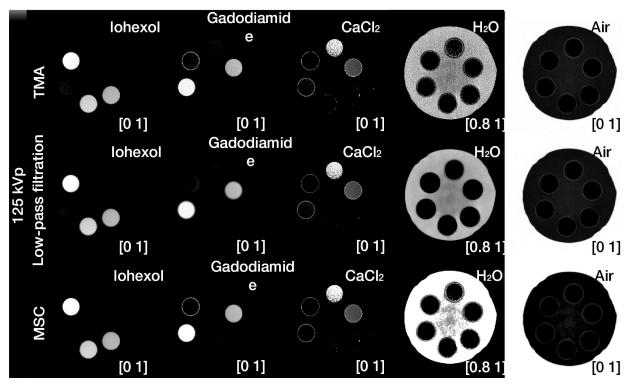


Fig. 9. The decomposition results from top row to bottom row using the methods of TMA (the 1st row), low-pass filtration (the 2nd row) and MSC using 125 kVp (the 3rd row). The material type from left to right is iohexol (the 1st column), gadodiamide (the 2nd column), calcium chloride (the 3rd column), water (the 4th column) and air (the 5th column). The display windows are on the bottom right of each column.

TABLE IV

The Means and STDs of Decomposed Images Within Each ROI in the Four-Material Phantom Study (# of Photons = 1×10^4)

Met	Methods		$\delta = 1.5 \times 10^{-06}$	$\delta = 1.5 \times 10^{-08}$	$\delta = 1.5 \times 10^{-09}$
ROI1	Bone	1±0	1±0	1±0	1±0
ROI2	Muscle	1 ± 0	1±0	0.958 ± 0.125	0.947 ± 0.134
ROI3	Adipose	1 ± 0	1±0	0.99 ± 0.07	0.989 ± 0.073
ROI4	Adipose	0.5 ± 0	0.535 ± 0.018	0.551 ± 0.318	0.547 ± 0.321
KO14	Muscle	0.5 ± 0	0.465 ± 0.018	0.449 ± 0.318	0.453 ± 0.321
ROI5	Air	1 ± 0	1±0	1±0	1±0
Mean STD		0.0060	0.1387	0.1414	

TV norm and higher decomposition accuracy using the L_0 norm.

TABLE V
THE MEANS AND NOISE STDS OF THE VOLUME FRACTION WITHIN
THE ROIS OF THE WATER PHANTOM WITH IGC INSERTS

Method			125 kVp			
		Truth	TMA	Low-pass filtration	MSC	
ROI1	Iohexol	1±0	0.989 ± 0.026	0.999 ± 0.004	1±0	
ROI2	Gadodiamide	1±0	0.958 ± 0.033	0.964 ± 0.005	1±0	
ROI3	Calcium chloride	1±0	0.807±0.236	0.822±0.152	0.899±0.167	
ROI4	Water	1±0	0.937 ± 0.019	0.936 ± 0.004	1±0	
DOIS	Iohexol	0.8 ± 0	0.824 ± 0.026	0.825 ± 0.009	0.819 ± 0.008	
ROI5	Water	0.2 ± 0	0.176 ± 0.026	0.177 ± 0.009	0.181 ± 0.008	
DOI/	Iohexol	0.7 ± 0	0.705±0.027	0.705 ± 0.012	0.7 ± 0.01	
ROI6	Water	0.3 ± 0	0.295 ± 0.027	0.296 ± 0.013	0.3 ± 0.01	
ROI7	Gadodiamide	0.7 ± 0	0.705 ± 0.049	0.703 ± 0.031	0.701 ± 0.019	
	Calcium chloride	0.3±0	0.295±0.049	0.294±0.035	0.299±0.019	
VFA			94.94%	95.30%	97.73%	
Average STD			0.0519	0.0274	0.0241	

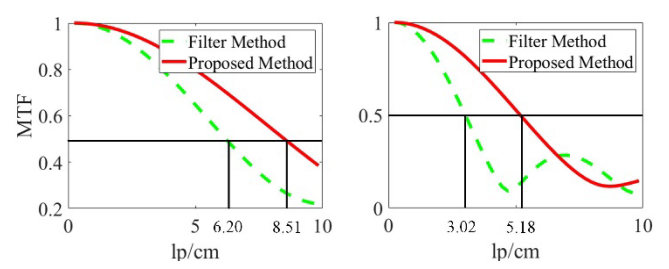


Fig. 10. MTF curves measured on the bone and muscle.

The typical MTFs of iohexol solution and gadodiamide solution using the low-pass filtration and MSC methods are calculated and plotted in Fig. 10. The spatial resolution using the proposed MSC method is increased by an overall factor of 1.56 at the MTF magnitude decreased to 50% compared with that using the low-pass filtration method.

2) Water Phantom With IG Inserts: The CT images of water phantom with the IG inserts and the contrast-free pure water phantom are shown in Figs. 11(a) and (b). The decomposed material images are shown in the 2nd row in Fig. 11. By applying Eq. (35), we acquire the VNC image as shown in Fig. 11(c). We plot the 1-D drawing of CT image of contrast-enhanced, contrast-free and VNC image of the customized water phantom as shown in Fig. 12. The VNC image using the proposed method is faithfully consistent with the contrast-free CT image (i.e., the ground-truth image). We achieve the RMSRE of 0.23% compared with the ground truth. The above observations show the high decomposition accuracy of the proposed method.

In Fig. 11(d), the CT number difference between the contrast-free image and VNC image is mainly concentrated around the boundary of the plastic water container and test tube. The reason is that the material edge is composed of pixels with LAC between water and test tube and the proposed method decomposes these pixels into water incorrectly.

C. Patient Study

The CT images of the abdominal slice are shown in Fig. 13. We select the ROIs of the blood vessel (the rectangle areas

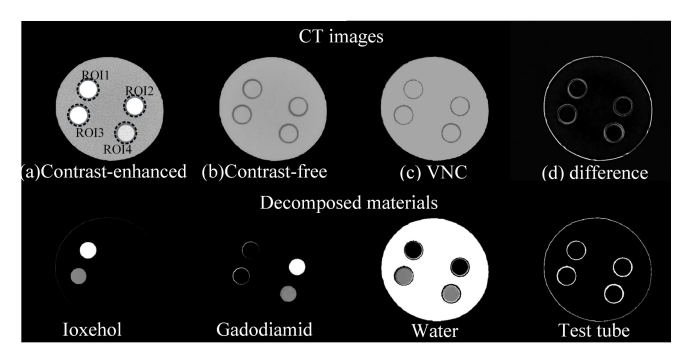


Fig. 11. The first row is the CT image of (a) contrast-enhanced, (b) contrast-free and (c) VNC of the customized water phantom. Display windows of (a), (b) and (c) are [0.015 0.025] mm⁻¹. (d) is the difference image between the contrast-free (b) and VNC (c) images and the display window is [0 0.004] mm⁻¹. The second row is the decomposed material of ioxehol solution, gadodiamide solution, water and test tube using the proposed method. Display windows are [0 1] for all the subfigures.

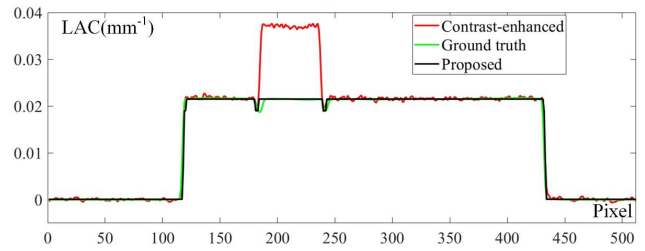


Fig. 12. The 1-D plot of CT image of contrast-enhanced, contrast-free and VNC image of the customized water phantom.

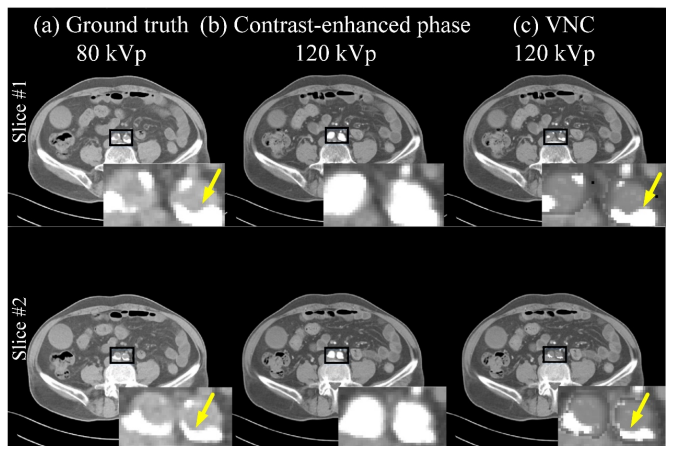


Fig. 13. The CT images of (a) ground-truth contrast-free phase, (b) contrast-enhanced phase and (c) VNC. The top and the bottom rows show the CT images of abdominal slice #1 and #2 of the patient. The display window is [0 650] HU for all.

as shown in Fig. 13) to perform the material decomposition on the contrast-enhanced CT image (Fig. 13(b)). By applying Eq. (35), we acquire the VNC image as shown in Fig. 13(c). The blood vessel areas are enlarged in the zoom-in display. In the contras-enhanced image, we cannot determine the calcification and its area. The calcification area can be clearly visualized in the VNC image. The calcification area in the VNC image has a similar shape to that in the ground-truth contrast-free CT image. The above observation shows that the proposed method successfully removes the contrast agent from the contrast-enhanced images to better visualize the calcification.

As pointed by the arrow in Fig. 13, the calcification area boundary in the VNC image is not strictly consistent to that in the ground-truth contrast-free CT image. The reasons are mainly two-fold. First of all, as the time lag of a few seconds exists between the contrast-free and contrast-enhanced phases, the anatomy within the two phases are not completely consistent due to the organ motion in the scanning time interval. Secondly, the material boundary is composed of pixels with LAC between the calcification and contrast agent. The proposed method may decompose these pixels into contrast agent material incorrectly.

V. DISCUSSION

We propose an image-domain MMD method for SECT using material sparsity constraint. The objective function contains a least-square data fidelity term and three regularization terms. The first regularization term is the TV norm which is applied according to the piece-wise constant property of the decomposed material image. The second regularization term is the L_0 norm of the material image to meet the material sparsity constraint within the human body. The third regularization term is a characteristic function designed to satisfy the sumto-one and box constraints of the decomposition. The above problem is non-convex due to the introduction of L₀ norm. We applied the APD algorithm with a line-search scheme to solve the problem. To obtain a good initial estimation of the non-convex problem, we apply matrix inversion assisted by the assumption that each pixel contains at most two material and perform the decomposition pixel by pixel.

The innovation of this work is mainly two-fold. Firstly, we introduce the concept of material sparsity into the decomposition to enhance the decomposition accuracy. Achieving MMD from single energy CT is an ill-posed problem since multiple unknowns need to be estimated from one set of measurements. Desired results cannot be achieved if no additional information is added. We apply material sparsity constraint into the decomposition and select L₀ norm as an embodiment of material sparsity due to its definition of counting the number of non-zero elements in one vector. Prior to this work, most MMD methods focus on suppressing the decomposition noise or increasing the decomposition spatial resolution in MMD [33], [43], [44]. Nevertheless, the decomposition accuracy is not increased in these methods since no additional information is added to solve the ill-posed MMD. By introducing the material sparsity into the MMD, we enhance the decomposition accuracy significantly according to our result in the phantom and patient studies.

Secondly, we achieve accurate multi-material decomposition using SECT as an alternative to the clinical application where DECT or spectral CT is not readily available. Before working on our SECT project, we have performed a careful literature review on the topic of material decomposition using SECT and found that the most related papers all perform two-material decomposition using SECT [31], [32]. In clinical applications, more than two-material images are usually required. For instance, liver-fat quantification requires a four-material differentiation: liver tissue, blood, fat, and contrast agent [15], [17]. The proposed method, which achieves more than

two material decomposition using SECT image, is thus attractive in clinical practice. We have applied the proposed method on the virtual non-contrast imaging to demonstrate its clinical relevance. The calcification area can be clearly visualized in the virtual non-contrast image generated by the proposed method, and has a similar shape to that in the ground-truth contrast-free CT image. The proposed method is thus feasible and promising in clinical applications.

Although the proposed method has achieved promising results, there are several aspects for future improvement. In the current algorithm, the proposed method is evaluated using the digital phantom, the water phantoms, and patient VNC data. In further clinical application, complicated tissue composition is an obstacle to the choice of material bases. We will apply the material dictionary concept proposed in refs. [3], [4] to include the major basis materials and develop an automatic scheme to select the material bases in future patient studies.

According to the nonconvex property of L_0 norm, there is a potential risk that the proposed method might stuck near the initial if the initial value is far from the optimal. We have evaluated the potential risk using three distinct levels of initial values (zero, 50% TMA, and 100% TMA) in the four- and five-material digital phantom studies. It turns out that the local minimum trap risk only occurs when zero value is applied in the five-material phantom study. The ill-posed characteristic of L₀ regularization might increase the risk of local minimum with the increment of the number of material bases, since more unknowns are needed to be estimated from one set of measurements. We will focus on the investigation of two schemes to mitigate the local minimum risk using L₀ optimization. The first one is to find a substitution of L₀ norm, including the relaxed approximation model [57], [58], fractional norm [59]–[61] and learning-based schemes [62], [63] which are shown to be effective in general signal processing [57], [58], [62], [63]. The other scheme is to provide desired initial values by integrating additional prior information, including the predetermined material composition according to the physician's delineation, into the initial estimation [53].

We would point out that, SECT cannot replace the clinical applications of DECT. For instance, SECT cannot distinguish the materials of very close or even equal LACs in specific energy in image domain. In the round digital phantom study, we find that the critical relative LAC difference value to achieve accurate material decomposition using the proposed method is 7.1%. Therefore, the proposed image-domain method using SECT is complementary to the clinical application and environment where DECT technique is not readily available. In our further study, we will extend the proposed image-domain MMD method to line integral to tackle for the above issue of failing to differentiate the materials with very close or equal LACs in specific energy spectrum since it has been demonstrated that the effective beam energy of each ray in the measured line integral can be used to differentiate the materials with different elemental compositions represented by the same CT number [64].

In our current implementation, within each voxel, a maximum of two material composition is assumed due to the physics constrains of data measurement and volume or mass

conservation. When the number of material bases is more than two within one voxel or rod, a taken-one-out iterative scheme might be developed. Supposing that N materials exist within one voxel. We can select one arbitrary base material and consider the other (N-1) mixture as one pseudo base material. The current two-material decomposition scheme can be applied to separate the one from (N-1) base materials. The same scheme repeats until all the N base materials are decomposed.

TV regularization is currently selected as one embodiment of noise suppression schemes in this work since our intention is to design the L₀ norm regularization to enforce the material sparsity constraint and decomposition accuracy in the MMD for SECT. Nevertheless, the piecewise constant property using TV regularization in the phantom study may not hold in more sophisticated patient evaluation since the phantom image contains little textures, making noise reduction more readily achievable without loss of texture. In our future study, we will apply advanced noise suppression schemes, e.g., BM3D (block-matching 3D Transform [65]) and learning-based methods [66]-[68], to the patient data to achieve delicate texture maintenance. We will also perform intensive comparison study on the performance of TV norm and other delicate texture maintenance schemes in clinical applications.

The MSC method is implemented in the image domain which is advantageous and more practical for clinics than DECT. However, the image domain method is prone the beam-hardening issues and the decomposition accuracy may be decreased. Future studies will extend the proposed method into the projection domain to construct a non-linear inversion model to reconstruct basis materials directly from the projection data and to reduce the beam-hardening artifacts simultaneously [24], [26]. In addition, scatter artifacts are commonly observed in CT images, especially in CBCT since the scatter photons increases with the enlarged illumination. The scatter artifacts contaminate the CT images and lead to incorrect decomposition. We presently narrow the collimation between the x-ray source and the object to limit the cone angle to reduce the scatter photons. We will further apply effective scatter correction schemes to decrease the scatter artifacts in the future [69], [70].

VI. CONCLUSION

In this paper, we propose an image-domain MMD method for SECT which integrate the material sparsity, represented by the L_0 norm regularization on the volume fraction, into the material decomposition model to achieve accurate multimaterial decomposition using SECT as an alternative technique to the clinical application where DECT or spectral CT is not readily available. The proposed method is validated using the phantom and patient studies. Compared with the TMA method, the proposed MSC method increases the VFA by 7.1% and decreases the noise STD by 85.1% in the phantom study. In the patient study, the calcification area can be clearly visualized in the virtual non-contrast image generated by the proposed method, and has a similar shape to that in the ground-truth contrast-free CT image. The high decomposition

quality using the proposed method substantially facilitates the SECT-based MMD clinical applications.

APPENDIX

A. Conjugate of Function for

The conjugate of a function h is defined as:

$$h^*(\vec{x}) = \sup_{\vec{w}} (\langle \vec{x}, \vec{w} \rangle - h(\vec{w})), \tag{36}$$

where $\langle \blacksquare, \blacksquare \rangle$ denotes the inner product, *sup* indicates the supremum. The conjugate of $f_2 = \delta \| \overrightarrow{z_2} \|_1$ can be written

$$f_{2}^{*}(\overrightarrow{z_{2}}) = \sup_{\overrightarrow{w_{2}}} \left(\langle \overrightarrow{z_{2}} \overrightarrow{w_{2}} \rangle - f_{2}(\overrightarrow{w_{2}}) \right)$$

$$= \sup_{\overrightarrow{w_{2}}} \left(\langle \overrightarrow{z_{2}} \overrightarrow{w_{2}} \rangle - \delta \| \overrightarrow{w_{2}} \|_{1} \right)$$

$$= \delta \sup_{\overrightarrow{w_{2}}} \left(\left\langle \frac{\overrightarrow{z_{2}}}{\delta}, \overrightarrow{w_{2}} \right\rangle - \| \overrightarrow{w_{2}} \|_{1} \right) 0. \tag{37}$$

If $\left\| \frac{\overrightarrow{z_2}}{\delta} \right\|_{\infty} \le 1$, we have:

$$\left\langle \frac{\overrightarrow{z_2}}{\delta}, \overrightarrow{w_2} \right\rangle - \left\| \overrightarrow{w_2} \right\|_1 \le \overrightarrow{w_2} - \left\| \overrightarrow{w_2} \right\|_1$$

$$= \sum_{i} \left(\overrightarrow{w_2} \right)_i - \sum_{i} \left| \left(\overrightarrow{w_2} \right)_i \right| \le 0 \quad (38)$$

and thus

$$f_2^*\left(\overrightarrow{Z_2}\right) = \delta_{\overline{w_2}}^{\sup}\left(\left\langle\frac{\overrightarrow{z_2}}{\delta}, \overrightarrow{w_2}\right\rangle - \left\|\overrightarrow{w_2}\right\|_1\right) = 0 \tag{39}$$

If $\left\| \frac{\overrightarrow{z_2}}{\delta} \right\|_{\infty} > 1$, $\left\langle \frac{\overrightarrow{z_2}}{\delta}, \overrightarrow{w_2} \right\rangle \to \infty$ and thus $f_2^* \left(\overrightarrow{z_2} \right) = \infty$. Therefore, the conjugate of f_2 is written as:

$$f_2^* \left(\overrightarrow{z_2} \right) = \begin{cases} 0 & if \ \|\overrightarrow{z_2}\|_{\infty} \le \delta \\ \infty & otherwise \end{cases}$$
 (40)

B. Proximal Map of Conjugate Function f₁*

Using Moreau decomposition in Eq. (21), the proximal map of f_1^* can be written as:

$$prox_{sf_1^*}(\overrightarrow{w_1}) = \overrightarrow{w_1} - s \times prox_{s^{-1}f_1}(\frac{\overrightarrow{w_1}}{s})$$
 (41)

By plugging the definition of f_1 (Eq. (14-1)) into the proximal operator of f_1 , we write $prox_{s^{-1}f_1}\left(\frac{\overrightarrow{w_1}}{s}\right)$ as:

$$prox_{s^{-1}f_{1}}\left(\frac{\overrightarrow{w_{1}}}{s}\right)$$

$$= \underset{\overrightarrow{z_{1}}}{argmin}\left(\frac{1}{2} \left\|\overrightarrow{z_{1}} - \overrightarrow{\mu}\right\|_{2}^{2} + \frac{s}{2} \left\|\overrightarrow{z_{1}} - \frac{\overrightarrow{w_{1}}}{s}\right\|_{2}^{2}\right)$$

$$= \underset{\overrightarrow{z_{1}}}{argmin}\left(\left(\frac{1}{2} + \frac{s}{2}\right)\overrightarrow{z_{1}}^{2} - (\overrightarrow{w_{1}} + \overrightarrow{\mu})\overrightarrow{z_{1}} + \frac{1}{2}\overrightarrow{\mu}^{2} + \frac{\overrightarrow{w_{1}}^{2}}{2s}\right)$$

$$= \frac{\overrightarrow{w_{1}} + \overrightarrow{\mu}}{1 + s}$$

$$(42)$$

By plugging Eq. (42) into Eq. (41), we acquire the proximal map of f_1^* as:

$$prox_{sf_1^*}(\overrightarrow{w_1}) = \frac{\overrightarrow{w_1} - s\overrightarrow{\mu}}{1+s}$$
 (43)

ACKNOWLEDGMENT

The authors would like to thank the editors and anonymous referees for their constructive comments, which significantly strengthen the paper. They also thank Ms. Qihui Lyu and Dr. Ke Sheng at the Department of Radiation Oncology, University of California, Los Angeles, for the helpful discussion on the derivation of conjugate functions and proximal maps. They also thank Mr. Ye Zhang in the Information Technology Center, Zhejiang University for his technical assistance on computational hardware support.

REFERENCES

- [1] P. R. S. Mendonça et al., "Multi-material decomposition of spectral CT images," Proc. SPIE, vol. 7622, no. 3, Mar. 2010, Art. no. 76221W.
- R. E. Alvarez and A. Macovski, "X-ray spectral decomposition imaging system," U.S. Patent 4029 963, Jun. 14, 1977.
- C. Shen, B. Li, L. Chen, M. Yang, Y. Lou, and X. Jia, "Material elemental decomposition in dual and multi-energy CT via a sparsitydictionary approach for proton stopping power ratio calculation," Med. Phys., vol. 45, no. 4, pp. 1491–1503, Apr. 2018, doi: 10.1002/mp.12796.
- C. Shen, B. Li, Y. Lou, M. Yang, L. Zhou, and X. Jia, "Multienergy element-resolved cone beam CT (MEER-CBCT) realized on a conventional CBCT platform," Med. Phys., vol. 45, no. 10, pp. 4461-4470, Oct. 2018, doi: 10.1002/mp.13169.
- [5] E. Y. Sidky, Y. Zou, and X. Pan, "Impact of polychromatic X-ray sources on helical, cone-beam computed tomography and dual-energy methods," Phys. Med. Biol., vol. 49, no. 11, p. 2293, 2004.
- [6] F. Kelcz, P. M. Joseph, and S. K. Hilal, "Noise considerations in dual
- energy CT scanning," *Med. Phys.*, vol. 6, no. 5, pp. 418–425, Sep. 1979. W. A. Kalender, E. Klotz, and L. Kostaridou, "An algorithm for noise suppression in dual energy CT material density images," IEEE Trans. Med. Imag., vol. MI-7, no. 3, pp. 218-224, Sep. 1988.
- E. O. Crawley, W. D. Evans, and G. M. Owen, "A theoretical analysis of the accuracy of single-energy CT bone-mineral measurements," Phys. Med. Biol., vol. 33, no. 10, p. 1113, 1988.
- [9] B. J. Kis, Z. Sarnyai, R. Kákonyi, M. Erdélyi, and G. Szabó, "Singleenergy material decomposition using X-ray path length estimation," J. Comput. Assist. Tomogr., vol. 36, no. 6, pp. 768-777, 2012.
- Y. Shao, Y. Gao, Q. Wang, X. Yang, and D. Shen, "Locally-constrained boundary regression for segmentation of prostate and rectum in the planning CT images," Med. Image Anal., vol. 26, no. 1, pp. 345-356, Dec. 2015, doi: 10.1016/j.media.2015.06.007
- [11] X. Ren et al., "Interleaved 3D-CNNs for joint segmentation of smallvolume structures in head and neck CT images," Med. Phys., vol. 45, no. 5, pp. 2063-2075, May 2018, doi: 10.1002/mp.12837.
- P. Stenner, T. Berkus, and M. Kachelrieß, "Empirical dual energy calibration (EDEC) for cone-beam computed tomography," Med. Phys., vol. 34, no. 9, pp. 3630-3641, Sep. 2007, doi: 10.1118/1.27691,04.
- [13] T. Wang and L. Zhu, "Dual energy CT with one full scan and a second sparse-view scan using structure preserving iterative reconstruction (SPIR)," Phys. Med. Biol., vol. 61, no. 18, pp. 6684-6706, Sep. 2016, doi: 10.1088/0031-9155/61/18/6684.
- [14] K. Müller et al., "Interventional dual-energy imaging-feasibility of rapid kV-switching on a C-arm CT system," Med. Phys., vol. 43, no. 10, pp. 5537-5546, Oct. 2016, doi: 10.1118/1.4962929.
- [15] D. Lee et al., "A feasibility study of low-dose single-scan dualenergy cone-beam CT in many-view under-sampling framework," IEEE Trans. Med. Imag., vol. 36, no. 12, pp. 2578-2587, Dec. 2017, doi: 10.1109/tmi.2017.2765760.
- [16] C. Maaß, E. Meyer, and M. Kachelrieß, "Exact dual energy material decomposition from inconsistent rays (MDIR)," Med. Phys., vol. 38, no. 2, pp. 691-700, Feb. 2011, doi: 10.1118/1.3533686.
- T. Johnson, C. Fink, S. O. Schönberg, and M. F. Reiser, "Dual energy CT in clinical practice," Med. Phys., vol. 38, no. 11, p. 6346, 2011.
- M. Petrongolo and L. Zhu, "Single-scan dual-energy CT using primary modulation," IEEE Trans. Med. Imag., vol. 37, no. 8, pp. 1799-1808, Aug. 2018, doi: 10.1109/tmi.2018.2796858.
- Y. Liao et al., "Pseudo dual energy CT imaging using deep learningbased framework: Basic material estimation," Proc. SPIE, vol. 10573, Mar. 2018, Art. no. 105734N.
- W. Zhao et al., "A deep learning approach for dual-energy CT imaging using a single-energy CT data," Proc. SPIE, vol. 11072, May 2019, Art. no. 1107222.

- [21] H. Yu et al., "Image gradient L₀-norm based PICCS for swinging multisource CT reconstruction," Opt. Exp., vol. 27, no. 4, pp. 5264-5279, Feb. 2019, doi: 10.1364/oe.27.005264.
- [22] W. Zhang, Y. Cao, R. Zhang, L. Li, and Y. Wen, "Image denoising via L_0 gradient minimization with effective fidelity term," Math. Problems Eng., vol. 2015, Dec. 2015, Art. no. 712801, doi: 10.1155/2015/ 712801.
- [23] W. Huang, W. Bi, G. Gao, Y. P. Zhang, and Z. Zhu, "Image smoothing via a scale-aware filter and L_0 norm," *IET Image Process.*, vol. 12, no. 9, pp. 1521–1528, Sep. 2018, doi: 10.1049/iet-ipr.2017.0719.
- [24] B. Chen, Z. Zhang, E. Y. Sidky, D. Xia, and X. Pan, "Image reconstruction and scan configurations enabled by optimization-based algorithms in multispectral CT," Phys. Med. Biol., vol. 62, no. 22, pp. 8763-8793, Nov. 2017, doi: 10.1088/1361-6560/aa8a4b.
- [25] Y. Malitsky and T. Pock, "A first-order primal-dual algorithm with linesearch," SIAM J. Optim., vol. 28, no. 1, pp. 411-432, Jan. 2018.
- [26] Y. Long and J. A. Fessler, "Multi-material decomposition using statistical image reconstruction for spectral CT," IEEE Trans. Med. Imag., vol. 33, no. 8, pp. 1614-1626, Aug. 2014, doi: 10.1109/tmi.2014.2320284.
- T. Niu and L. Zhu, "Accelerated Barrier optimization compressed sensing (ABOCS) reconstruction for cone-beam CT: Phantom studies," Med. Phys., vol. 39, no. 7, pp. 4588-4598, Jul. 2012.
- [28] L. R. Rabiner, "A tutorial on hidden Markov models and selected applications in speech recognition," Proc. IEEE, vol. 77, no. 2, pp. 257-286, Feb. 1989, doi: 10.1109/5.18626.
- [29] D. Gabay and B. Mercier, "A dual algorithm for the solution of nonlinear variational problems via finite element approximation," Comput. Math. Appl., vol. 2, no. 1, pp. 17-40, 1976.
- [30] E. Strekalovskiy and D. Cremers, "Real-time minimization of the piecewise smooth Mumford-Shah functional," in Proc. Eur. Conf. Comput. Vis. (ECCV). Cham, Switzerland: Springer, 2014, pp. 127-141.
- [31] T. Möllenhoff, E. Strekalovskiy, M. Moeller, and D. Cremers, "Low rank priors for color image regularization," in Energy Minimization Methods in Computer Vision and Pattern Recognition. Cham, Switzerland: Springer, 2015, pp. 126-140.
- [32] Z. Xu, S. De, M. Figueiredo, C. Studer, and T. Goldstein, "An empirical study of ADMM for nonconvex problems," 2016, arXiv:1612.03349. [Online]. Available: http://arxiv.org/abs/1612.03349
- [33] Q. Ding, T. Niu, X. Zhang, and Y. Long, "Image-domain multimaterial decomposition for dual-energy CT based on prior information of material images," Med. Phys., vol. 45, no. 8, pp. 3614-3626, Aug. 2018, doi: 10.1002/mp.13001.
- [34] N. Parikh and S. Boyd, "Proximal algorithms," Found. Trends Optim., vol. 1, no. 3, pp. 127-239, Jan. 2014, doi: 10.1561/2400000003.
- [35] T. Blumensath and M. E. Davies, "Iterative thresholding for sparse approximations," J. Fourier Anal. Appl., vol. 14, nos. 5-6, pp. 629-654, Dec. 2008
- [36] A. Kyrillidis, S. Becker, V. Cevher, and C. Koch, "Sparse projections onto the simplex," in Proc. Int. Conf. Mach. Learn., 2013, pp. 235-243.
- Y. Chen and X. Ye, "Projection onto a simplex," 2011, arXiv:1101.6081. [Online]. Available: http://arxiv.org/abs/1101.6081
- [38] P. L. Combettes and V. R. Wajs, "Signal recovery by proximal forward-backward splitting," Multiscale Model. Simul., vol. 4, no. 4, pp. 1168-1200, Jan. 2005, doi: 10.1137/050626090.
- [39] P. V. Granton, S. I. Pollmann, N. L. Ford, M. Drangova, and D. W. Holdsworth, "Implementation of dual- and triple-energy cone-beam micro-CT for postreconstruction material decomposition," Med. Phys., vol. 35, no. 11, pp. 5030-5042, Nov. 2008, doi: 10.1118/1.2987668
- [40] T. P. Szczykutowicz and G.-H. Chen, "Dual energy CT using slow kVp switching acquisition and prior image constrained compressed sensing," Phys. Med. Biol., vol. 55, no. 21, pp. 6411-6429, Nov. 2010, doi: 10.1088/0031-9155/55/21/005.
- [41] Y. Jiang et al., "Noise suppression in image-domain multi-material decomposition for dual-energy CT," IEEE Trans. Biomed. Eng., vol. 67, no. 2, pp. 523-535, Feb. 2020.
- [42] P. Lamb, D. V. Sahani, J. M. Fuentes-Orrego, M. Patino, A. Ghosh, and P. R. S. Mendonca, "Stratification of patients with liver fibrosis using dual-energy CT," IEEE Trans. Med. Imag., vol. 34, no. 3, pp. 807-815,
- [43] Y. Xue et al., "Image domain multi-material decomposition using single energy CT," Phys. Med. Biol., vol. 65, no. 6, Mar. 2020, Art. no. 065014, doi: 10.1088/1361-6560/ab7503.
- Y. Xue et al., "Statistical image-domain multimaterial decomposition for dual-energy CT," Med. Phys., vol. 44, no. 3, pp. 886-901, Mar. 2017.

- [45] M. A. T. Figueiredo, R. D. Nowak, and S. J. Wright, "Gradient projection for sparse reconstruction: Application to compressed sensing and other inverse problems," IEEE J. Sel. Topics Signal Process., vol. 1, no. 4, pp. 586–597, Dec. 2007, doi: 10.1109/jstsp.2007.910281. Siemens. Accessed: Aug. 30, 2020. [Online]. Available: https://bps-
- healthcare.siemens.com/cv_oem/radIn.asp
- NIST. X-Ray Mass Attenuation Coefficients. Accessed: Sep. 10, 2020. [Online]. Available: https://www.nist.gov/pml/x-ray-mass-attenuationcoefficients
- [48] A. C. Kak and M. Slaney, Principles of Computerized Tomographic Imaging. Philadelphia, PA, USA: SIAM, 2001, p. 22.
- [49] F. Natterer, The Mathematics of Computerized Tomography,
 B. G. Teubner, Ed. Philadelphia, PA, USA: SIAM, 2001, pp. 107–108.
- [50] W. Zhao, D. Li, K. Niu, W. Qin, H. Peng, and T. Niu, "Robust beam hardening artifacts reduction for computed tomography using spectrum modeling," IEEE Trans. Comput. Imag., vol. 5, no. 2, pp. 333-342, Jun. 2019, doi: 10.1109/tci.2018.2884479.
- [51] R. A. Rutherford, B. R. Pullan, and I. Isherwood, "X-ray energies for effective atomic number determination," Neuroradiology, vol. 11, no. 1, pp. 23-28, May 1976.
- [52] P. C. Johns and M. J. Yaffe, "Theoretical optimization of dual-energy X-ray imaging with application to mammography," Med. Phys., vol. 12,
- no. 3, pp. 289–296, 1985. [53] Y. Xue *et al.*, "Accurate multi-material decomposition in dual-energy CT: A phantom study," IEEE Trans. Comput. Imag., vol. 5, no. 4,
- pp. 515–529, Dec. 2019, doi: 10.1109/tci.2019.2909192. [54] S. Richard, D. B. Husarik, G. Yadava, S. N. Murphy, and E. Samei, "Towards task-based assessment of CT performance: System and object MTF across different reconstruction algorithms," Med. Phys., vol. 39, no. 7, pp. 4115–4122, 2012.
- [55] E. Samei, M. J. Flynn, and D. A. Reimann, "A method for measuring the presampled MTF of digital radiographic systems using an edge test
- device," *Med. Phys.*, vol. 25, no. 1, pp. 102–113, 1998. [56] P. R. S. Mendonca, P. Lamb, and D. V. Sahani, "A flexible method for multi-material decomposition of dual-energy CT images," IEEE Trans. Med. Imag., vol. 33, no. 1, pp. 99-116, Jan. 2014.
- [57] S. Wang, D. Liu, and Z. Zhang, "Nonconvex relaxation approaches to robust matrix recovery," presented at the 23rd Int. Joint Conf. Artif. Intell., Beijing, China, 2013.
- M. Morup, K. H. Madsen, and L. K. Hansen, "Approximate L_0 constrained non-negative matrix and tensor factorization," in *Proc. IEEE*
- Int. Symp. Circuits Syst., vols. 1–10, May 2008, pp. 1328–1331. [59] S. Foucart and M.-J. Lai, "Sparsest solutions of underdetermined linear systems via ℓ_q -minimization for $0 < q \leqslant 1$," Appl. Comput. Harmon. Anal., vol. 26, no. 3, pp. 395–407, May 2009. [60] C. Miao and H. Yu, "Alternating iteration for $l_p(0$
- regularized CT reconstruction," IEEE Access, vol. 4, pp. 4355-4363, 2016
- [61] Z. Xu, X. Chang, F. Xu, and H. Zhang, " $L_{1/2}$ regularization: A thresholding representation theory and a fast solver," IEEE Trans. Neural Netw. Learn. Syst., vol. 23, no. 7, pp. 1013-1027, Jul. 2012.
- Y. Yang, J. Feng, N. Jojic, J. Yang, and T. S. Huang, "Subspace learning by ℓ^0 -induced sparsity," Int. J. Comput. Vis., vol. 126, no. 10, pp. 1138-1156, Oct. 2018, doi: 10.1007/s11263-018-1092-4
- [63] J. Li, K. Yu, and F. Yun, "Sparse subspace clustering by learning approximation ℓ_0 codes," in Proc. AAAI Conf. Artif. Intell., 2017, pp. 2189-2195.
- [64] Y. Li et al., "Feasibility of achieving spectral CT imaging from a single KV acquisition and deep learning method," Proc. SPIE, vol. 11312, Mar. 2020, Art. no. 1131222
- [65] A. Danielyan, V. Katkovnik, and K. Egiazarian, "BM3D frames and variational image deblurring," IEEE Trans. Image Process., vol. 21, no. 4, pp. 1715–1728, Apr. 2012, doi: 10.1109/tip.2011.
- [66] H. Chen et al., "LEARN: Learned experts' assessment-based reconstruction network for sparse-data CT," IEEE Trans. Med. Imag., vol. 37, no. 6, pp. 1333-1347, Jun. 2018, doi: 10.1109/tmi.2018.2805692.
- Q. Yang et al., "Low-dose CT image denoising using a generative adversarial network with Wasserstein distance and perceptual loss," IEEE Trans. Med. Imag., vol. 37, no. 6, pp. 1348-1357, Jun. 2018, doi: 10.1109/tmi.2018.2827462
- [68] C. You et al., "Structurally-sensitive multi-scale deep neural network for low-dose CT denoising," IEEE Access, vol. 6, pp. 41839-41855, 2018, doi: 10.1109/access.2018.2858196.
- [69] P. Wu et al., "Iterative CT shading correction with no prior information," Phys. Med. Biol., vol. 60, no. 21, pp. 8437-8455, Nov. 2015, doi: 10.1088/0031-9155/60/21/8437.
- [70] C. Yang et al., "Shading correction assisted iterative cone-beam CT reconstruction," Phys. Med. Biol., vol. 62, no. 22, pp. 8495–8520, Oct. 2017, doi: 10.1088/1361-6560/aa8e62.